

***Suzaku* Observations of Local Ultraluminous Infrared Galaxies**

Stacy H. Teng <sup>1,2</sup>, Sylvain Veilleux <sup>2</sup>, Naohisa Anabuki <sup>3</sup>, Charles D. Dermer <sup>4</sup>,  
 Luigi C. Gallo <sup>5</sup>, Takao Nakagawa <sup>6</sup>, Christopher S. Reynolds <sup>2</sup>, D.B. Sanders <sup>7</sup>,  
 Yuichi Terashima <sup>8</sup>, and Andrew S. Wilson <sup>2</sup>

**ABSTRACT**

We report the results from our analysis of *Suzaku* XIS (0.5–10 keV) and HXD/PIN (15–40 keV) observations of five well-known local ULIRGs: *IRAS* F05189–2524, *IRAS* F08572+3915, Mrk 273, PKS 1345+12, and Arp 220. The XIS observations of F05189–2524 and Mrk 273 reveal strong iron lines consistent with Fe K $\alpha$  and changes in spectral shapes with respect to previous *Chandra* and *XMM-Newton* observations. Mrk 273 is also detected by the HXD/PIN at  $\sim 1.8\sigma$ . For F05189–2524, modeling of the data from the different epochs suggests that the change in spectral shape is likely due to the central source switching off, leaving behind a residual reflection spectrum, or an increase in the absorbing column. An increase in the covering fraction of the absorber can describe the spectral variations seen in Mrk 273, although a reduction in the intrinsic AGN luminosity cannot be formally ruled out. The *Suzaku* spectra of Mrk 273 are well fit by a  $\sim 94\%$  covering fraction model with a column density of  $\sim 10^{24}$  cm<sup>-2</sup>. The absorption-corrected  $\log[L_{2-10 \text{ keV}}/L_{\text{IR}}]$  ratio is consistent with those found

---

<sup>1</sup>Contacting author: stacyt@astro.umd.edu.

<sup>2</sup>Department of Astronomy, University of Maryland, College Park, MD 20742, U.S.A.

<sup>3</sup>Department of Earth and Space Science, Osaka University, 1-1 Machikaneyama Toyonaka, Osaka 560-0043, Japan

<sup>4</sup>Space Science Division, Code 7653, U.S. Naval Research Laboratory, Washington, D.C. 20375-5352, U.S.A.

<sup>5</sup>Department of Astronomy and Physics, Saint Mary's University, Halifax, NS B3H 3C3, Canada

<sup>6</sup>Institute of Space and Astronautical Science, Japan Aerospace Exploration Agency, 3-1-1 Yoshinodai, Sagami-hara, Kanagawa 229-8510, Japan

<sup>7</sup>Institute for Astronomy, University of Hawaii, 2680 Woodlawn Drive, Honolulu, HI 96822, U.S.A.

<sup>8</sup>Department of Physics, Ehime University, Matsuyama, Ehime 790-8577, Japan

in PG Quasars. The change in the spectral shape on a time scale of a few years implies that the absorbing matter must be near the AGN ( $\sim 1$  pc). The 0.5–10 keV spectrum of PKS 1345+12 and Arp 220 seem unchanged from previous observations and their hard X-ray emission is not convincingly detected by the HXD/PIN. The large column density derived from CO observations and the large equivalent width of an ionized Fe line in Arp 220 can be reconciled by an ionized reflection model. F08572+3915 is undetected in both the XIS and HXD/PIN, but the analysis of unpublished *Chandra* data provides a new measurement at low energies.

*Subject headings:* galaxies: active — galaxies: individual: IRAS F05189–2524, IRAS F08572+3915, Mrk 273, PKS 1345+12, Arp 220 — galaxies: starburst — X-rays: galaxies

## 1. Introduction

Ultraluminous Infrared Galaxies (ULIRGs) are galaxies with  $L_{\text{IR}} = L_{8-1000\mu\text{m}} \geq 10^{12}L_{\odot}$ , equivalent to the minimum bolometric luminosity of QSOs. The discovery of a large population of local ULIRGs is one of the most important legacies of the *IRAS* satellite. At luminosities above  $10^{12}L_{\odot}$ , the space density of ULIRGs in the local universe is greater than that of optically selected quasars with similar bolometric luminosity by a factor of  $\sim 1.5$  (Sanders & Mirabel 1996). Thus ULIRGs represent the most common type of galaxy at these high luminosities. Systematic ground-based and space-based optical and near-infrared imaging studies have shown that local ULIRGs are almost always undergoing mergers (e.g., Sanders et al. 1988; Veilleux et al. 2002, 2006). Sanders et al. (1988) suggested that these objects represent a dust-enshrouded phase that eventually evolves into optically-selected quasars. If this is true, ULIRGs take on a fundamental importance for the origin and evolution of quasars.

The primary energy source — active galactic nucleus (AGN) versus starburst activity — of ULIRGs is still under debate. Optical and infrared observations show that most local ULIRGs are dominated by starbursts, but about 30% show evidence of AGNs (Veilleux et al. 1999a,b). Furthermore, the “warm” infrared colors ( $f_{25\mu\text{m}}/f_{60\mu\text{m}} > 0.2$ ) and quasar-like spectra of the more luminous objects imply that active nuclei are significant in these objects (e.g., Veilleux et al. 1995, 1999a,b, 2008; Genzel et al. 1998; Tran et al. 2001; Armus et al. 2007). These results would be definitive if it were not for the possibility of severe obscuration.

Galaxy mergers cause massive in-falls of gaseous material towards the center of ULIRGs (e.g., Rupke, Veilleux, & Baker 2008), and column densities  $\gtrsim 10^{24} \text{ cm}^{-2}$  have been deduced from CO measurements (e.g., Downes & Solomon 1998; Evans et al. 2002). Observations at UV, optical, near-infrared, and even mid-infrared wavelengths may therefore not always probe the cores of these objects. High resolution ( $\ll 1''$ ), high frequency radio observations can penetrate high columns and are an excellent probe of whether an AGN is present (e.g., Lonsdale, Smith, & Lonsdale 1993). However, the bolometric luminosity in the radio band is insignificant, so radio data cannot test whether accretion onto a supermassive black hole (SMBH) is the dominant energetic process. We are left with hard X-rays.

Recent surveys with *XMM-Newton* and *Chandra* (e.g. Ptak et al. 2003; Franceschini et al. 2003; Teng et al. 2005) have found that  $\sim 40\%$  of observed ULIRGs show signatures of AGNs. The observed 2–10 keV luminosity of the surveyed sample is  $\sim 10^{40} - 10^{43} \text{ ergs s}^{-1}$ , with a majority of the sources having luminosities below  $10^{42} \text{ ergs s}^{-1}$ . While the ratio  $\log[L_{2-10 \text{ keV}}/L_{\text{IR}}]$  is small in nearby ULIRGs (from  $-4$  to  $-1$ ; e.g., Teng et al. 2005), this is not much smaller than that found in radio-quiet QSOs (from  $-3$  to  $-1$ ). Moreover, absorption may be a factor even at these energies. If the absorbing column exceeds  $\sim 10^{24} \text{ cm}^{-2}$ , the primary continuum emission is suppressed significantly by absorption and Compton down-scattering. Thus observations at  $\gtrsim 10 \text{ keV}$  are best to detect Compton-thick AGNs. The sensitivity of *Suzaku* at these high energies is well suited for the study of highly obscured sources like ULIRGs.

In this paper, we present *Suzaku* XIS (0.5–10 keV) and HXD/PIN (15–40 keV) observations of five well-known local ULIRGs. In §2, we discuss our sample. In §3, we report the observations and describe the methods we used to reduce the data. In §4, the results from our spectral analysis of the *Suzaku* data are discussed. In §5, we combine the *Suzaku* data with earlier published and unpublished *XMM-Newton* and *Chandra* data to fine tune our spectral models. The results of this study are summarized in §6. Throughout this paper, we adopt the cosmology of  $H_0=75 \text{ km s}^{-1} \text{ Mpc}^{-1}$ ,  $\Omega_M=0.3$ , and  $\Omega_\Lambda=0.7$ .

## 2. Sample

The five ULIRGs in the present study are *F05189–2524*, *F08572+3915*, Mrk 273, PKS 1345+12, and Arp 220. They were selected because they have readily available *Suzaku* data, either from our own program (PI: Veilleux) or from the public archive. They are among the nearest, brightest, and best-studied ULIRGs in the *IRAS* Bright Galaxy Survey (Sanders et al. 2003). Table 1 lists the basic properties of these sources. Here we briefly review the relevant literature on each source.

*F05189–2524* is an unresolved late stage merger surrounded by tidal debris (Veilleux et al. 2002, 2006) with “warm” infrared colors. It is optically classified as a Seyfert 2, but near-infrared spectroscopy of this source reveals the presence of an obscured broad line region (BLR) at  $\text{Pa}\alpha$  (Veilleux et al. 1999a, b). Spectra from previous *ASCA* (Risaliti et al. 2000; Severgnini et al. 2001), *XMM-Newton* (Imanishi & Terashima 2004), and *Chandra* (Ptak et al. 2003) observations flatten out above 2 keV and are best fit by an absorbed power law with  $N_{\text{H}} \sim 0.5 - 1 \times 10^{23} \text{ cm}^{-2}$ ,  $\Gamma \sim 1.0-1.9$ , and a thermal component with  $kT \sim 0.1-0.9 \text{ keV}$ . The absorption-corrected 2–10 keV luminosity derived from the published *XMM-Newton* and *Chandra* data is  $\sim 10^{43} \text{ ergs s}^{-1}$ .

*F08572+3915* is another “warm” ULIRG, consisting of a pair of interacting galaxies with nuclear separation of  $\sim 6 \text{ kpc}$  (Veilleux et al. 2002, and references therein). The northwestern nucleus is classified as a LINER. A 2-cm radio core coincides with the northwestern nucleus (Nagar et al. 2003). However, only an upper limit on its 2–10 keV flux exists in the literature –  $7.6 \times 10^{-12} \text{ ergs cm}^{-2} \text{ s}^{-1}$  – from the *HEAO* satellite (Polletta et al. 1996).

Mrk 273 is in the early phase of a merger where the nuclei are separated by 680 pc (Veilleux et al. 2002) and is optically classified as a Seyfert 2 (Veilleux et al. 1999a). A [Si VI]  $1.96 \mu\text{m}$  feature, a strong indicator of AGN activity, is detected in this “cool” ULIRG (Veilleux et al. 1999b). Its radio flux falls above the radio-to-FIR correlation of starbursts and a bright AGN-like radio core is detected on VLBA scale in this object (Lonsdale et al. 1993). The *Chandra* 0.5–2 keV X-ray spectrum of Mrk 273 is best explained with a MEKAL plasma with  $kT \sim 1.3 \text{ keV}$  and its 2–10 keV spectrum is best fit by an absorbed power law with  $\Gamma \sim 1.0$  and  $N_{\text{H}} \sim 10^{23} \text{ cm}^{-2}$  (Ptak et al. 2003). The flat slope of the 2–10 keV continuum may be a result of reflection, but the *Chandra* observation of Ptak et al. (2003) shows a very weak Fe  $K\alpha$  emission line with an equivalent width of  $\sim 0.09-0.44 \text{ keV}$ . Comparisons of observations by *ASCA*, *BeppoSAX*, and *Chandra* show that this source exhibits possible long term flux variability (Xia et al. 2002).

PKS 1345+12 is yet another “warm” ULIRG. It is in the early stage of a merger with two nuclei separated by 4.0 kpc (Veilleux et al. 2002). Optically classified as a Seyfert 2 galaxy (Sanders et al. 1988; Kim et al. 1998), infrared observations by Veilleux et al. (1997) suggest a buried BLR at  $\text{Pa}\alpha$ . Observations by Evans et al. (1999) have shown that the eastern nucleus has colors consistent with reddened starlight while the the western nucleus has extremely red colors indicative of an optical quasar. The western nucleus is also coincident with peak CO emission (Evans et al. 1999), a radio core (Nagar et al. 2003), and 0.5–8 keV X-ray emission (Imanishi & Terashima 2004). According to Imanishi & Terashima (2004), the *Chandra* continuum is consistent with that of an absorbed AGN (power law  $\Gamma=1.8$  with  $N_{\text{H}} \sim 4.5 \times 10^{22} \text{ cm}^{-2}$ ). The *Chandra* data also showed a narrow Fe  $K\alpha$  emission line with an

equivalent width of  $\sim 0.13$  keV.

Finally, Arp 220 is by far the best-studied ULIRG due to its vicinity. Optically classified as a LINER, this “cool” ULIRG is also an early merger with nuclei separated by  $\sim 0.4$  kpc (Veilleux et al. 2002). Multi-wavelength data suggest the presence of a black hole in the western nucleus (Downes & Eckart 2007, and references therein). Previous *Chandra* observations detected both nuclei as well as extended soft X-ray emission from lobes and plumes that extend beyond the optical galaxy (Clements et al. 2002; McDowell et al. 2003). The full *Chandra* band nuclear spectrum is best fit by a thermal MEKAL component with  $kT \sim 0.8$  keV and a flat power law with  $\Gamma \sim 1.1$  absorbed by a column of  $\sim 10^{21}$  cm $^{-2}$  (Ptak et al. 2003). Analysis of *XMM-Newton* data by Iwasawa et al. (2005) suggests the presence of an Fe K emission line with equivalent width of  $\sim 1.9$  keV emanating from the western nucleus.

### 3. Observations and Data Reduction

The details of the *Suzaku* observations are listed in Table 2. Three of the sources (*F05189–2524*, Mrk 273, and PKS 1345+12) were of our own program (PI: Veilleux, Anabuki was co-PI for *F05189–2524*) and the other two, *F08572 + 3915* (PI: Gallagher) and Arp 220 (PI: the *Suzaku* Science Working Group, or SWG), were downloaded from the public archive. All of the observations were performed at the HXD aim point to increase the sensitivity of the HXD. The analysis of the data on *F05189–2524*, *F08572+3915*, Mrk 273, and Arp 220 was performed with version 6.3.1 of HEASoft and CALDB version 20071016. PKS 1345+12 was observed at the end of Cycle 2 and after the completion of the data analysis on the other objects in the sample. Thus, the analysis of the data on PKS 1345+12 was performed with the more up-to-date version 6.4 of HEASoft and CALDB version 20080401.

#### 3.1. XIS Data Reduction

The XIS data reduction followed the guidelines provided in the *Suzaku* Data Reduction Guide<sup>1</sup>. The data were screened following the version 2 data screening criteria. Due to nearby field sources, cleaned events for all objects except PKS 1345+12 were then extracted in circular regions with 1’ radii (the minimum recommended region size) centered on the targets wherever possible. The PKS 1345+12 field is rather empty, so the extraction region has a radius of  $\sim 3.1'$ . Since the extraction regions are so large, *Chandra* ACIS data were

---

<sup>1</sup>See <http://heasarc.gsfc.nasa.gov/docs/suzaku/analysis/abc/>.

used as a check to ensure no other X-ray sources were included in the extraction regions. Background events were extracted in same-sized nearby source-free regions. The source spectra were binned to at least 50 counts  $\text{bin}^{-1}$  for PKS 1345+12 and at least 15 counts  $\text{bin}^{-1}$  for the others so that  $\chi^2$  statistics can be used when modeling the spectra.

The response (RMF) and auxiliary (ARF) files were produced using `xisrmfgen` and `xissimarfgen`. The ARF files were generated assuming 400,000 incident photons and the default grid spacing.

In the modeling of the XIS data, the XIS1, XIS2, and XIS3 detectors are assumed to have the data processing version 2.0 cross-normalization factors of 1.065, 1.035, and 1.067 with respect to the XIS0 detector, respectively<sup>2</sup>.

### 3.2. HXD/PIN Data Reduction

The HXD/PIN data were reduced following the guidelines provided by the *Suzaku* team. The HXD/PIN spectra for both sources were extracted after the selection of good time intervals (the “ANDed GTI” from both the data and the non-X-ray background provided by the *Suzaku* HXD team). Dead-time corrections (on the order of about 5%) were applied to the extracted source spectra. The extracted spectra were binned using `grppha`<sup>3</sup>.

The response files were provided by the HXD team. Due to changes in the bias voltages and the threshold over time, we used the first-epoch response file for observations of *F05189–2524*, *F08572+3915*, and Arp 220, second-epoch for Mrk 273, and fourth-epoch for PKS 1345+12.

As its name implies, the non-X-ray backgrounds (NXB) from charged particles modeled by the HXD team do not include the cosmic X-ray background (CXB) which peaks within the energy range of the HXD/PIN. The CXB for each galaxy was modeled following a recipe<sup>4</sup> provided by the HXD team. The simulated CXB is approximately 5% of the NXB. The NXB and CXB were added together using `mathpha` to provide total backgrounds for the HXD/PIN data.

---

<sup>2</sup>See: <ftp://legacy.gsfc.nasa.gov/suzaku/doc/xrt/suzakumemo-2007-11.pdf>

<sup>3</sup>We binned the data using group 0 31 2 32 63 4 64 95 8 96 127 32 128 255 64. Each set of three numbers represent the channel range grouped and the number of channel bins in each group. This choice of grouping was used so that each bin contains approximately the same number of photons.

<sup>4</sup>See: [http://heasarc.gsfc.nasa.gov/docs/suzaku/analysis/pin\\_cxb.html](http://heasarc.gsfc.nasa.gov/docs/suzaku/analysis/pin_cxb.html).

At the time of this writing, the accuracy of the processing version 2.0 HXD/PIN background model is 3.8%<sup>5</sup>. However, a  $\sim 10\%$  offset in the version 2.0 background model was discovered for data taken between March and May of 2006 due to changes in the PIN observing mode. For the affected data (*F05189–2524* and *F08572+3915*), processing version 1.2 HXD/PIN background were used as recommended by the *Suzaku* team. Dead time corrections were also performed on the backgrounds for the affected data<sup>6</sup>. The reproducibility of the version 1.2 background is between 5 and 10%<sup>7</sup>. For the modeling of the data, the cross-normalization of the PIN with respect to XIS0 is 1.16 and 1.13 for the version 1.2 and 2.0 backgrounds, respectively<sup>8</sup>.

#### 4. *Suzaku* Results

The spectra were analyzed using the XSPEC package (version 11.3.2ag). The energy range of the detectors were limited to 0.5–10 keV for the XIS detectors and 15–40 keV for the PIN detector to avoid calibration problems. All the errors in the parameters are at the 90% level for one parameter of interest ( $\Delta\chi^2 = 2.7$ ).

In the modeling of the spectra, a simple power-law distribution absorbed only by the Galactic column is first assumed. If the model is not a satisfactory fit to the data, then more components are added on to the model until a satisfactory fit is achieved. The continuum model components considered in this paper are: (1) an absorbed power-law model which represents emission from an AGN (model parameters fitted include a column density,  $N_{\text{H}}$ , a power law index,  $\Gamma$ , and a normalization factor), (2) a thermal MEKAL model representing emission from stars or galactic winds (with a gas temperature,  $kT$ , and a normalization factor), (3) a partial-covering fraction model where some fraction,  $f_{\text{cover}}$ , of the intrinsic nuclear radiation is absorbed and the rest goes through unimpeded. The other parameters fitted are the equivalent column density,  $N_{\text{H}}$ ,  $\Gamma$ , and a normalization factor. (4) a scattering model where an absorbed power law represents the direct transmitted component and an unabsorbed power law of the same photon index represents a scattered component ( $N_{\text{H}}$ ,  $\Gamma$ , and a normalization factor for each of the direct and scattered components), (5) a

---

<sup>5</sup>This is the  $1\text{-}\sigma$  statistical plus systematic error in the 15–40 keV band for a net integration time of 10 ksec. See: <ftp://legacy.gsfc.nasa.gov/suzaku/doc/hxd/suzakumemo-2007-09.pdf>.

<sup>6</sup>See: <http://www.astro.isas.ac.jp/suzaku/analysis/hxd/v1/pinnxb/>

<sup>7</sup>See: <ftp://legacy.gsfc.nasa.gov/suzaku/doc/hxd/suzakumemo-2006-43.pdf>.

<sup>8</sup>See: <ftp://legacy.gsfc.nasa.gov/suzaku/doc/xrt/suzakumemo-2006-40.pdf> for version 1.2 backgrounds and [suzakumemo-2007-11.pdf](ftp://legacy.gsfc.nasa.gov/suzaku/doc/hxd/suzakumemo-2007-11.pdf) for version 2.0 backgrounds.

neutral reflection model<sup>9</sup> with an unabsorbed power law representing the direct component and a reflection component with the same photon index as the direct component ( $\Gamma$  and a normalization factor for each of the reflected and transmitted components), and finally, (6) a pure ionized reflection model as proposed by Ross & Fabian (2005) without any direct transmitted component ( $\Gamma$  and a normalization factor).

#### 4.1. IRAS F05189–2524

##### 4.1.1. XIS Spectrum

The XIS spectrum of *F05189–2524* is shown in Figure 1. First, we find that it is well-modeled by a simple power-law model plus a MEKAL component with abundances fixed at solar all modified by Galactic absorption ( $\chi^2_\nu = 1.57$  for 124 degrees of freedom). An additional Gaussian component is needed ( $\Delta\chi^2=22.8$  for a change in d.o.f. of 3) to reproduce the emission line at  $\sim 6.4$  keV (*i.e.* the Fe  $K\alpha$  line; equivalent width, or EW,  $\sim 1.84$  keV). While the spectrum shows excess emission at around 1.3 and 1.9 keV (Si XIII emission features), the addition of a second and a third Gaussian component to the model does not significantly improve the fit ( $\Delta\chi^2=0.05$  for a change in d.o.f. of 3). The excess emission at 1.9 keV may be a calibration feature associated with absorption edges from the mirror. The relatively flat spectral index and the large equivalent width of the iron line suggest that the spectrum may be reflection dominated. The addition of a reflection component to the continuum model results in a better fit ( $\chi^2_\nu = 1.49$  for 123 d.o.f.). The *F*-test probability for the addition of one parameter (the normalization of the reflected component) is relatively small, at  $1.6 \times 10^{-2}$ , implying that it is reasonable to add the extra component. While the spectral index required for this fit,  $\Gamma = 2.68^{+0.30}_{-0.13}$ , is unusually steep for an AGN where the canonical value for  $\Gamma$  is  $\sim 1.8$ , it is not too different from the range seen in PG quasars (1.3–2.48; Piconcelli et al. 2005). The best-fit reflection model parameters to the XIS spectrum are listed in Table 3 and the best-fit model is shown with the spectrum in Figure 1.

---

<sup>9</sup>The reflection component is represented by the PEXRAV model in XSPEC. For the spectral fitting, the metal abundance, iron abundance, and inclination angle are fixed at the default value. The relative reflection parameter is fixed at  $-1$ , thus modeling only the reflection component. No energy cut off is assumed. Therefore, only  $\Gamma$  and the normalization factor are free parameters.



#### 4.1.2. HXD/PIN Data

*F05189–2524* is undetected by the HXD/PIN. As mentioned in § 3.2, the documentation provided by the *Suzaku* team state that the reproducibility of the version 1.2 HXD/PIN backgrounds are on average  $\sim 5\text{--}10\%$ . Here we estimate the systematic and statistical error of the HXD/PIN data for our specific observation. The standard deviation of the histogram of the 15–40 keV residuals from the 1-day (40 ksec) observations in the documentation imply that the systematic error of the NXB is  $\sim 2.4\%$ . Considering the net HXD/PIN integration time and the 15–40 keV total background count rate for observations with integration times longer than 40 ksec, the statistical error of the *F05189-2524* observation is  $\sim 0.9\%$ . Thus, the total  $1\text{-}\sigma$  error (systematic and statistical errors added in quadrature) for the HXD/PIN observation of *F05189-2524* is  $\sim 2.6\%$ . Therefore, the 15–40 keV  $3\text{-}\sigma$  detection limit for this observation is  $\sim 0.020$  counts per second (cps).

### 4.2. IRAS F08572+3915

#### 4.2.1. XIS Non-Detection and XMM-Newton and Chandra Data

As mentioned previously in § 2, there has never been a published X-ray detection of *F08572+3915* in the X-ray energy range. It is also undetected by the XIS. A constraint on the limiting flux of *F08572+3915* can be derived from the background. The average background count rate from the XIS front illuminated detectors (XIS0, 2, 3) is  $\sim 1.3 \times 10^{-3}$  cps. Assuming an ideal, flat background ( $\Gamma \sim 1$ ), the **WebPIMMS**<sup>10</sup> application was used to estimate the observed flux of the background spectrum. The application yields a flux of  $\sim 4 \times 10^{-14}$  ergs s<sup>-1</sup> cm<sup>-2</sup>, more than two orders of magnitude better than the upper limit placed on this object by *HEAO*.

*F08572+3915* was observed with both *XMM-Newton* and *Chandra*, but the results of the analysis were never published. *F08572+3915* is undetected in the archived *XMM-Newton* data (ObsID: 0200630101, PI: Imanishi,  $t_{\text{effective}}=13$  ksec). But the lower background and better spatial resolution of the *Chandra* ACIS-S archival data (ObsID: 6862, PI: Komossa,  $t_{\text{effective}}=15$  ksec) provide a conclusive detection of nine counts in the 0.5–8 keV band. The *Chandra* detection coincides with the optical northwestern nucleus (*i.e.* the LINER/Seyfert 2 nucleus). Assuming a canonical AGN power law spectrum ( $\Gamma=1.8$ ) modified by Galactic absorption for the Seyfert 2 nucleus, the detected count rate of *F08572+3915* in the *Chandra*

---

<sup>10</sup><http://heasarc.gsfc.nasa.gov/Tools/w3pimms.html>

band corresponds to an observed 0.5–10 keV flux of  $\sim 5 \times 10^{-15}$  ergs s $^{-1}$  cm $^{-2}$ . This estimate is consistent with the upper limit derived from the XIS observations.

The *Chandra* detection implies that the Seyfert nucleus may be a weak X-ray source or a heavily obscured AGN. If we assume no intrinsic absorption, the 0.5–10 keV flux from the *Chandra* observation of this object implies an intrinsic luminosity of  $\sim 5 \times 10^{40}$  ergs s $^{-1}$ . This luminosity falls within the range of X-ray luminosities of LINERs as measured by Terashima & Wilson (2003) and is consistent with LINERs being powered by low-luminosity AGNs.

However, like many other LINER 2s (Terashima & Wilson 2003), *F08572+3915* is likely to be affected by absorption. Infrared observations of this object do show strong absorption features and weak PAH emission characteristic of deeply buried AGNs with a line-of-sight extinction of  $A_V \geq 78$  mag. (Imanishi et al. 2006; Armus et al. 2007; Veilleux et al. 2008). A CO-based estimate of the column density by Evans et al. (2002) is in the range of  $\sim 3$ – $10 \times 10^{24}$  cm $^{-2}$ . The hardness ratio of the *F08572+3915* detection is 0.56. Following the hardness ratio method presented in Teng et al. (2005), a single power law with an estimated photon index of  $\sim -0.43$  would fit the data. The inverted power law spectrum may be an indication of a large column density since the softer 0.5–2 keV photons are more readily affected by absorption. The estimated 0.5–10 keV flux from the hardness ratio method, which assumes Galactic absorption only, is  $2.61 \times 10^{-13}$  ergs s $^{-1}$  cm $^{-2}$ , corresponding to a luminosity of  $\sim 2 \times 10^{42}$  ergs s $^{-1}$ .

#### 4.2.2. HXD/PIN Data

*F08572+3915* is not detected by the HXD/PIN above the total background. Following the procedure outlined in § 4.1.2, the HXD/PIN 3- $\sigma$  detection limit was used to approximate the limiting count rate and observed flux in the 15–40 keV band. The 3- $\sigma$  upper limit on the count rate for *F08572+3915* in the HXD/PIN band is  $\sim 0.020$  cps.

### 4.3. Mrk 273

#### 4.3.1. XIS Spectrum

Mrk 273 is detected by the XIS. We first tried to model the XIS spectrum with a MEKAL component describing the starburst and a heavily absorbed power-law distribution which does not fit the 2–10 keV spectrum properly. Rather, the XIS spectrum is well

modeled by the scattering model plus a MEKAL component with abundances fixed at solar and all components modified by Galactic absorption. Approximately 9% of the intrinsic AGN emission is scattered. An additional Gaussian component is needed to model the emission line at  $\sim 6.4$  keV (EW $\sim 0.56$  keV). While the spectrum shows excess emission at around 1.9 keV (Si XIII emission), the addition of a second Gaussian component to the model does not significantly improve the fit ( $\Delta\chi^2=1$  with  $\Delta\text{d.o.f.}=3$ ). Again, the feature at 1.9 keV may be a calibration feature associated with absorption edges from the mirror. A reflection model was also tested on the XIS spectrum, but this results in a worse fit ( $\chi^2_\nu = 1.52$  for 187 d.o.f.) than the scattering model ( $\chi^2_\nu = 1.25$  for 187 d.o.f.). The best-fit parameters to the XIS spectrum are listed in Table 3 and the XIS spectrum with the best-fit model is shown in Figure 1.

#### 4.3.2. HXD/PIN Data & Contaminants

Mrk 273 is marginally detected by the HXD/PIN. The net (observed minus background) HXD/PIN spectrum of Mrk 273 is  $\sim 5.4\%$  of the total (NXB+CXB) background. Figure 2 is a comparison of the spectrum, total background, and net spectrum. The current best estimate for the error in the version 2.0 NXB background is 3.8% for observations with net integration time of 10 ksec. We estimate the error on our Mrk 273 observation following the steps outlined in §4.1.2. The total systematic plus statistical error for the Mrk 273 observation is  $\sim 3.0\%$ , implying the HXD/PIN detection of Mrk 273 is at  $\sim 1.8\text{-}\sigma$  (or with  $\sim 93\%$  confidence).

Because the PIN is not an imaging detector and has a very large field of view ( $34' \times 34'$ ,  $\sim 3.5$  times the area of the XIS field of view), there may be sources of contamination in the HXD/PIN signal. While hard X-ray and soft gamma ray catalogs (e.g. the INTEGRAL reference catalog; Ebisawa et al. 2003) do not list any sources of comparable flux within the PIN field of view and energy range, most of these flux values are based on modeling of previous observations at lower energies. There remains a possibility that the signal may come from a previously unobserved nearby source. Three likely candidates are detected within the field of view of the XIS. Mrk 273x is an unabsorbed Seyfert 2 galaxy at a redshift of 0.458 located approximately  $1.2'$  northeast of Mrk 273. The XIS spectrum of Mrk 273x is well fit by a power-law component modified only by Galactic absorption ( $\Gamma \sim 1.69^{+0.11}_{-0.12}$ ;  $\chi^2_\nu \sim 1.21$  for 77 d.o.f.). The observed 0.5–10 keV flux of Mrk 273 is approximately 2.9 times that of Mrk 273x. SBS 1342+560 is a background QSO at a redshift of 0.937 located approximately  $6.3'$  south of Mrk 273. The XIS spectrum of this source is also well fit by a power-law component modified only by Galactic absorption ( $\Gamma \sim 2.03 \pm 0.05$ ;  $\chi^2_\nu \sim 1.28$  for

242 d.o.f.). The observed 0.5–10 keV flux of Mrk 273 is approximately 1.5 times that of this source. Lastly, SDSS J1342512.06+554759.6 is a background QSO at a redshift of 1.17 located approximately 7' southeast of Mrk 273. Its XIS spectrum is once again well fit by a power-law component modified only by Galactic absorption ( $\Gamma \sim 1.62 \pm 0.07$ ;  $\chi^2_\nu \sim 1.29$  for 139 d.o.f.). The observed 0.5–10 keV flux of Mrk 273 is approximately 1.9 times that of this source.

Thus, none of the objects within the XIS field of view shows evidence of being highly obscured. One would therefore expect their spectral energy distributions at higher energies to follow the power law seen at low energies. If that is indeed the case, their contributions to the overall PIN signal of Mrk 273 are negligible; this is explained in the next section.

#### 4.3.3. Combined XIS-HXD/PIN Spectral Modeling

We modeled the combined XIS and PIN spectrum of Mrk 273 with the scattering model. All of the best-fit parameters are consistent with the values obtained from the fit of the XIS spectrum alone with the exception of the column density which increased by a factor of  $\sim 2$ . The HXD/PIN contributions from the neighboring sources have been taken into account by adding the best-fit XIS model of the contaminants to the HXD/PIN component of the Mrk 273 model (see Figure 3). The best-fit model to the full-band Mrk 273 spectrum in this case has parameter values listed in Table 3 and the spectrum is shown in Figure 4 with the XIS-HXD/PIN spectrum. While the photon index value of  $\sim 1.4$  may suggest flattening of the spectrum due to reflection, the addition of a reflection component resulted in a statistically worse fit ( $\chi^2_\nu = 1.66$  for 197 d.o.f.) relative to that obtained from the scattering model ( $\chi^2_\nu = 1.35$  for 199 d.o.f.). Approximately 5% of the intrinsic AGN flux is scattered. The gas temperature of  $\sim 0.7$  keV is consistent with the range found in ULIRGs (Grimes et al. 2005). Overall, the best-fit model of Mrk 273 agrees well with X-ray observations of other ULIRGs (e.g. Ptak et al. 2003; Franceschini et al. 2003; Teng et al. 2005, 2008). The comparison of the XIS data with published results is postponed until § 5.2.

## 4.4. PKS 1345+12

### 4.4.1. XIS Spectrum

The XIS spectrum of PKS 1345+12 is shown in Figure 1. It is best modeled by a scattering continuum model (§ 4) modified by Galactic absorption. The transmitted AGN flux is  $\sim 2\%$  of the intrinsic AGN flux. Unlike other ULIRGs, the 0.5–2 keV spectrum does

not require a MEKAL thermal component. The best-fit parameters are listed in Table 3. These best-fit values and the model of the 0.5–10 keV continuum are consistent with *Chandra* measurements reported by Imanishi & Terashima (2004). The Imanishi & Terashima (2004) model for the *Chandra* data includes a narrow Fe line at 6.4 keV. This emission line also appears in the XIS spectrum, but is statistically insignificant ( $\Delta\chi^2=2.0$  for a change in d.o.f. of 2). This is also consistent with the fact that the lower limit to the equivalent width of the Fe line in the Imanishi & Terashima (2004) model is 0 keV. No flux or spectral variation were detected over the 0.5–10 keV energy range between the *Chandra* and *Suzaku* observations.

The unabsorbed 0.5–10 keV flux for PKS 1345+12 is  $\sim 6.0 \times 10^{43}$  ergs s<sup>-1</sup> and the absorption corrected ratio  $\log[L_{2-10 \text{ keV}}/L_{\text{IR}}]$  is  $\sim -2.3$ , consistent with the range found in PG quasars. This and the lack of a thermal component in the 0.5–2 keV spectrum suggest that the X-ray spectrum is dominated by an AGN.

#### 4.4.2. HXD/PIN Data

The net HXD/PIN spectrum of PKS 1345+12 lies  $\sim 3.4\%$  above the total background (Figure 2). Accounting for the uncertainties in the PIN background of  $\sim 3.1\%$  (see § 4.1.2 on how this was calculated), the detection is at only  $1.1\sigma$ . There are not enough net counts for a meaningful spectral fitting of the full-band (XIS+HXD/PIN) spectrum. However, assuming no contamination from nearby sources, the net observed 15–40 keV count rate for PKS 1345+12 is  $9.9 \pm 2.8 \times 10^{-3}$  cps. Using the XIS best-fit model, given the lack of an obvious reflection component, the 15–40 keV count rate translates to a flux of  $\sim 4.4_{-1.3}^{+1.1} \times 10^{-12}$  ergs s<sup>-1</sup> cm<sup>-2</sup>.

### 4.5. Arp 220

#### 4.5.1. XIS Spectrum

Arp 220 is detected by the XIS. At first, the XIS spectrum was modeled by a simple power-law model plus a MEKAL component for the thermal contribution from the starburst. An additional Gaussian component is needed to reproduce the emission line at  $\sim 6.7$  keV (EW $\sim 1.98$  keV), which is consistent with emission from Fe XX–Fe XXVI. This model with only Galactic absorption is a satisfactory fit to the XIS data ( $\chi^2_{\nu} \sim 1.03$  for 174 d.o.f.). The XIS extraction window encompasses the two nuclei of Arp 220 and a significant fraction of the extended soft X-ray emission (McDowell et al. 2003). Nevertheless, the power-law plus MEKAL model to the XIS-only data are consistent with the results from the *Chandra*

observation of the nuclear binary source (Clements et al. 2002). There is, therefore, no obvious sign of spectral or flux variability in Arp 220.

The *Suzaku* data on Arp 220 can be interpreted in several ways: (1) an AGN is not present, (2) there is a low-luminosity, unobscured AGN, or (3) there is a heavily obscured AGN.

In the first case where an AGN is not present, the detected Fe line at  $\sim 6.7$  keV would originate from hot gas heated by the heavy starburst activity. However, the measured equivalent width for the line of  $1.98_{-0.57}^{+0.99}$  keV seems too large for an Fe emission line arising from a pure starburst. Iwasawa et al. (2005) fitted the 2.5–10 keV continuum of the *XMM-Newton* data with a collisionally ionized plasma model. The model requires a gas temperature of  $\sim 7$  keV and a metallicity of  $\sim 2$  times solar in order to reproduce the 6.7 keV Fe feature (EW  $\sim 2$  keV). This temperature is inconsistent with the detected Ca XIX line in the *XMM-Newton* data. The XIS data do suggest the presence of an emission feature at  $\sim 3.9$  keV consistent with Ca XIX, but this detection is not statistically significant.

The weak but unobscured AGN case is unlikely based on CO observations by Downes & Eckart (2007). Their observations with IRAM imply a column density of  $\sim 1.3 \times 10^{25}$  cm $^{-2}$  for the western nucleus of Arp 220. Unless the covering fraction of the absorber is much less than unity, the unobscured AGN interpretation of the data is inconsistent with the CO observations.

In contrast, the third scenario of a heavily obscured AGN is consistent with the Fe line detection and the CO observation of a large column density. The ionized reflection model as proposed by Ross & Fabian (2005, and references therein) can reconcile the large equivalent width of the highly ionized iron line as well as the large absorbing column. Since the absorbing column is so large, the observed spectrum is purely reflected. The XIS data is best fit by a MEKAL plus an ionized reflection model with the ionization parameter ( $\xi$ ) fixed at  $10^3$  ergs cm s $^{-1}$  ( $\chi^2_\nu = 1.03$  for 176 d.o.f.; see Table 3 and Figure 1). Thus the third scenario for explaining the *Suzaku* data on Arp 220 is favored.

Based solely on the XIS data, the unabsorbed 0.5–10 keV luminosity of Arp 220 is only  $\sim 1.8 \times 10^{41}$  ergs s $^{-1}$  cm $^{-2}$ , much lower than that found in quasars. The absorption-corrected ratio  $\log[L_{2-10 \text{ keV}}/L_{\text{IR}}]$  is  $\sim -4.9$ , consistent with those found in some nearby ULIRGs (Teng et al. 2005), but lower than those of radio-quiet quasars. Of course, if Arp220 is highly absorbed then the intrinsic  $\log[L_{2-10 \text{ keV}}/L_{\text{IR}}]$  is higher and may be within the range for PG quasars. The thermal component of the spectrum has a 0.5–2 keV luminosity of  $\sim 3 \times 10^{40}$  ergs s $^{-1}$ . If this luminosity is completely due to thermal bremsstrahlung, then applying this to Equation (1) of Teng et al. (2008), the spatial extent of the emitting region

is  $\sim 2 - 11$  kpc, depending on the choice of filling factor ( $10^{-3} < f_{gas} < 10^{-1}$ ) and assuming an electron density of  $1 \text{ cm}^{-3}$ .

#### 4.5.2. HXD/PIN Data

As shown in Figure 2, the net HXD/PIN spectrum of Arp 220 is only  $\sim 2.2\%$  above the (NXB+CXB) background, so it is within the uncertainties of the PIN background modeling ( $\sim 3.0\%$ , calculated following procedures in § 4.1.2). Thus, the estimated 15–40 keV count rate for Arp 220 is  $\sim 0.025$  cps.

### 5. The Long-term Variability of *IRAS F05189–2524* and Mrk 273

Within the span of the *Suzaku* observations ( $\sim 80$  ksec each), no significant variability is detected in the XIS data for both *F05189–2524* and Mrk 273. However, there is evidence for long-term variability in both sources when the *Suzaku* data are compared with previous *ASCA*, *BeppoSax*, *Chandra*, and *XMM-Newton* data. In this section, we discuss the results of these comparisons and their implications for the spectral models.

#### 5.1. *IRAS F05189–2524*

*F05189–2524* was observed by *XMM-Newton* in March 2001 and then by *Chandra* in October 2001 and January 2002. We extracted the spectra from the *XMM-Newton* and *Chandra* archives. There do not appear to be significant variations in the 0.5–2 keV flux of *F05189–2524*. The 2006 *Suzaku* measurement is within a standard deviation of the weighted average of the previous measurements. In contrast, the *Suzaku* 2–10 keV flux is a factor of  $\sim 30$  lower than the measurements made by other observatories,  $\sim 4$  standard deviations away from the weighted average of the previous measurements (see Figure 5 and 6).

None of the *XMM-Newton* and *Chandra* data shows a significant iron feature near 6.4 keV, in contrast to our more recent *Suzaku* data, so we did not consider reflection models for these archived data. The scattering model (§ 4) with a thermal MEKAL component gave adequate fits to the spectra. In the modeling of these data, we allowed the internal column density and the parameters for the power-law component describing the AGN within the source to vary freely. The models suggest that the archived *XMM-Newton* and the two sets of *Chandra* spectra are absorbed by a column density of  $7.6 \times 10^{22}$ ,  $6.8 \times 10^{22}$ , and  $6.1 \times 10^{22} \text{ cm}^{-2}$ , respectively. We also deduce that the observed 2–10 keV flux of the AGN has de-

creased from  $3 \times 10^{-12}$  ergs s $^{-1}$  cm $^{-2}$  in the 2001 *XMM-Newton* data to  $1 \times 10^{-13}$  ergs s $^{-1}$  cm $^{-2}$  in the 2006 *Suzaku* data *i.e.* a reduction of a factor of  $\sim 30$ .

The decrease in flux and the change in spectral shape may be due to a number of reasons. Here, we test three scenarios by modeling the multiple epoch data simultaneously with a single model. The three scenarios considered are: (1) a change in the column density while the properties of the AGN remain the same, (2) a change in the covering fraction of the absorber while the properties of the AGN remain the same, and (3) the column density and covering fraction remain the same while the intrinsic AGN luminosity is changed. In this scenario, a reflection component is visible in the “low-state” AGN.

The first scenario is tested by modeling all four data sets simultaneously by a single scattering model plus a MEKAL component modified only by Galactic absorption and a Gaussian describing the iron line. All of the model parameters are set to be the same for each of the data groups, except for the column density parameter which is allowed to vary independently. This results in a satisfactory fit to the data ( $\chi^2_\nu = 1.26$  for 503 d.o.f.). This model and the multi-epoch data are shown in Figure 7 and the best-fit parameters are listed in Table 4.

For the second scenario, the multi-epoch data are simultaneously fit by a single partial covering fraction model. All of the model parameters are set to be the same between epochs, except for the covering fraction. The modeling of this scenario results in an unacceptable fit with  $\chi^2_\nu \sim 8$ . The addition of another partial-covering absorber to this model results in a still unsatisfactory fit with  $\chi^2_\nu = 2.2$  for 498 degrees of freedom. Thus the partial-covering model is not a good description of the data.

Lastly, the third scenario is examined. In this scenario, the active nucleus has switched off prior to the final set of observations, leaving behind a residual reflection component visible in the “low” state. This has been observed previously in NGC 4051 (Guainazzi et al. 1998) and NGC 1365 (Risaliti et al. 2005). The model for this scenario is a combination of a MEKAL component, plus a reflection component on top of a scattering model. A Gaussian is also added to model the Fe line seen in the *Suzaku* data. For the *Suzaku*-epoch, the scattered component normalization is held fixed at zero. Similarly, for the non-*Suzaku*-epochs, the reflected component normalization is fixed at zero. Additionally, the absorption parameter in each of the non-*Suzaku*-epochs is allowed to vary independently while the *Suzaku*-epoch absorption parameter is held fixed at zero. Since the intrinsic AGN luminosity has changed, the normalization factors for the direct component are different for the *Suzaku*- and non-*Suzaku*-epochs. The modeling of the data with this scenario is rather successful with  $\chi^2_\nu = 1.30$  for 502 degrees of freedom. The best-fit parameters to this model are listed in Table 4 and the model shown in Figure 7.



Both the increase in column density and the decrease in intrinsic luminosity of the AGN appear to be equally good descriptions of the data. However, in the first scenario, the  $N_{\text{H}}$  value required to explain the data is  $> 2 \times 10^{24} \text{ cm}^{-2}$ . At this limit, we can no longer model it as a pure absorption spectrum since scattering both in and out of the line of sight are becoming important.

The thermal 0.5–2 keV luminosity is  $\sim 1 \times 10^{41} \text{ ergs s}^{-1}$ . Following the methods presented in § 4.5.1, the physical extent of the emitting region is  $\sim 4\text{--}17 \text{ kpc}$ ). The absorption-corrected 0.5–10 keV luminosity of the AGN detected in *F05189–2524* at its “high” state (2000–2002 observations) is  $\sim 3 \times 10^{43} \text{ ergs s}^{-1}$ , almost as luminous as some quasars (Elvis et al. 1994). The absorption-corrected ratio  $\log[L_{2\text{--}10 \text{ keV}}/L_{\text{IR}}]$  is  $\sim -2.5$ , consistent with that found in radio-quiet PG quasars. The corresponding numbers for the “low” state as observed by *Suzaku* are  $\sim 8 \times 10^{41} \text{ ergs s}^{-1}$  and  $-4.1$ , respectively, well below that of radio-quiet PG quasars.

## 5.2. Mrk 273

Xia et al. (2002) compiled a list of observed fluxes of Mrk 273 and Mrk 273x from *ASCA*, *BeppoSax*, and *Chandra* dating from 1994 to 2000<sup>11</sup>. We add to this list the *XMM-Newton* observation from 2002 analyzed by Balestra et al. (2005) and our *Suzaku* observation from 2006. Figure 8 shows the observed fluxes of Mrk 273 and Mrk 273x over the 12-year period. Since *ASCA* and *BeppoSax* did not have the spatial resolution to separate Mrk 273 from Mrk 273x, the flux points from 1994 and 1998 represent the sum of the two galaxies. As the figure shows, the total flux between Mrk 273 and Mrk 273x appears to have increased in 2006 in the 0.5–2 keV band and appears to be in a “high” flux state in 2000 relative to all the other measurements.

Although Mrk 273x was once thought to be a BL Lacertae object because of its high X-ray to optical B-band flux ratio (Xia et al. 1998), its 2–10 keV flux has never shown dramatic variability. The *Suzaku* data support the assessment of Xia et al. (2002) that Mrk 273x is unlikely to be a BL Lac object. As discussed in §4.3.2, its spectrum is well fit by a simple power law modified only by Galactic absorption, in agreement with the findings in Balestra et al. (2005).

Assuming a constant flux for Mrk 273x implies that the nominal observed 2–10 keV flux

---

<sup>11</sup>Although the authors tabulated the fluxes from 1996 to 2000, the *ASCA* observation date was misidentified and the data set was actually taken in December of 1994 (see Iwasawa 1999).

from Mrk 273 dropped by about a factor of two from 1994 to 1998, then increased by a factor of  $\sim 2.5$  from 1998 to 2000, and then again dropped by a factor of more than two from 2000 to 2002. It appears to have remained roughly the same from 2002 to 2006. This variability in flux is not very significant when considering the uncertainties of the measurements. However, the spectral variability is clearly seen when comparing the spectra of Mrk 273 from *Chandra*, *XMM-Newton*, and *Suzaku* (Figure 9). The higher 0.5–2 keV flux in 2006 and the higher 2–10 keV flux in 2000 as shown in Figure 8 correlate with the difference in the spectral shapes of the source in each of these epochs.

### 5.2.1. Modeling the Multiple Epoch Data

As with the multiple data sets of F05189–2524, we first modeled the archived *Chandra* and *XMM-Newton* spectra of Mrk 273 individually. These data sets were each best fit by the scattering model. The fits to the *Chandra* (*XMM-Newton*) data imply an intrinsic column density of  $4.1$  ( $6.8$ )  $\times 10^{23}$   $\text{cm}^{-2}$  and an intrinsic 2–10 keV flux of  $2.5$  ( $2.0$ )  $\times 10^{-12}$   $\text{ergs s}^{-2}$   $\text{cm}^{-2}$ . A comparison of the *Chandra* (*XMM-Newton*) data with the fits to the 2006 *Suzaku* XIS data in Table 3 suggests that the intrinsic column density has increased by  $\sim 110\%$  ( $\sim 27\%$ ) while the intrinsic 2–10 keV luminosity has decreased by  $\sim 80\%$  ( $0\%$ ) if we were to compare data only over the 0.5–10 keV range. However, the addition of the HXD/PIN data (Table 3) implies that the column density has increased by a factor of  $\sim 4$  ( $\sim 2$ ) and the intrinsic 2–10 keV luminosity has increased by a factor of  $\sim 3$  ( $\sim 4$ ).

Next, all three data sets are modeled with a single model simultaneously to determine whether the change in the spectral shape is due to the change in column density or the intrinsic AGN luminosity. Three scenarios are considered: the change in spectral shape is due to (1) a change in the absorbing column and the intrinsic AGN flux remains the same, (2) a change in the intrinsic AGN luminosity with the absorbing column remaining constant, and (3) a change in the covering fraction of the absorber with the column density and intrinsic luminosity remaining constant.

To evaluate the first scenario, all three data sets are simultaneously modeled by a scattering plus MEKAL model modified only by Galactic absorption and a Gaussian describing the iron line. All of the model parameters are set to be the same for all of the data groups, but the column density for data sets from each epoch is allowed to vary (assuming the intrinsic luminosity remains the same). As before, the contaminants in the HXD/PIN field of view are taken into account in the modeling. This interpretation of the data results in a poor fit ( $\chi^2_{\nu} = 1.76$  for 380 d.o.f.), much worse than the modeling to each data set alone and underestimates the flux of the HXD/PIN data (see Figure 10).

The second scenario is explored by again modeling the multi-epoch data simultaneously with a single model. The model is the same as that used in the first scenario. However, in this case, the model parameters for each epoch are set to be the same except for the normalization of the power law. In this case, we are testing whether the change in the intensity of the power-law component can describe the observations. The best-fit model for this scenario takes into account the contributions from the nearby contaminants. While the model describes the 0.5–10 keV data for each epoch well ( $\chi^2_\nu = 1.53$  for 378 d.o.f.), it fits the HXD/PIN data very poorly, severely under-estimating the HXD/PIN flux (see Figure 10).

To test the third scenario, the *Chandra*, *XMM-Newton*, and *Suzaku* spectra are modeled using two absorbers with the same column densities for data from each epoch but with covering fractions that are allowed to vary freely. The contributions to the HXD/PIN flux from the neighboring XIS sources are taken into account in the fitting of the *Suzaku* data. The best-fit model ( $\chi^2_\nu = 1.39$  for 376 d.o.f.) is shown in Figure 10 and the best-fit parameter values are listed in Table 4. Based on Figure 10, the third scenario is the preferred model for the multiple epoch data.

Using the parameters derived for this third scenario, the absorption-corrected luminosity from the AGN is  $4.0 \times 10^{43}$  ergs s<sup>-1</sup> in the 0.5–10 keV band and  $2.3 \times 10^{43}$  ergs s<sup>-1</sup> in the 15–40 keV band. The ratio  $\log[L_{2-10 \text{ keV}}/L_{\text{IR}}]$  is  $\sim -2.3$ , within the range found in radio-quiet PG quasars. The thermal 0.5–2 keV luminosity is  $\sim 1 \times 10^{40}$  ergs s<sup>-1</sup>. Following the methods discussed in § 4.5.1, the emission region is  $\sim 4$ –17 kpc in size.

Given the lack of knowledge of the detailed geometry of the nuclear region, it is difficult to derive a quantitative measure of the distance from the central source to the absorber. However, the year-to-year time variability suggests that the absorber is close ( $\sim 1$  pc) to the nucleus.

### 5.2.2. Comparison with OSSE Data

Dermer et al. (1997) observed Mrk 273 with the OSSE instrument on-board the *Compton Gamma Ray Observatory*. Though their observations resulted in a non-detection, they placed upper limits on the 50–100 keV band flux and the column density. Possible explanations suggested by Dermer et al. (1997) for the non-detection include the possibility that this ULIRG is gamma-ray weak or the AGN source is highly variable in gamma-rays and they happened to have observed the object in the low-flux state.

Another explanation for the non-detection is that the AGN in Mrk 273 is hidden behind a large and patchy column of gas  $\gtrsim 10^{24}$  cm<sup>-2</sup>. This is not inconsistent with the upper limit

derived from previous CO measurements ( $\lesssim 2 \times 10^{24} \text{ cm}^{-2}$ , assuming a covering fraction of unity; see Dermer et al. 1997 for more detail). These limits on the column density are consistent with our partial covering absorption model ( $N_{\text{H}} \sim 1.6 \times 10^{24} \text{ cm}^{-2}$ ). From an extrapolation of the HXD/PIN observation and model, we derive an upper limit to the 50–100 keV photon flux of  $6.2 \times 10^{-5} \text{ photons cm}^{-2}$  or  $6.9 \times 10^{-12} \text{ ergs s}^{-1} \text{ cm}^{-2}$ . This value is more stringent by a factor of  $\sim 2$  than the OSSE value ( $1.5 \times 10^{-4} \text{ photons cm}^{-2}$ ).

## 6. Summary

The results of our analysis of *Suzaku* XIS (0.5–10 keV) and HXD/PIN (15–40 keV) observations of five of the brightest and best-known local ULIRGs (*F05189–2524*, *F08572+3915*, Mrk 273, PKS 1345+12, and Arp 220) have been presented and compared with earlier *Chandra* and *XMM-Newton* data. The results can be summarized as follows:

1. The XIS observations of *F05189–2524* reveal a significant change in the observed 2–10 keV spectrum relative to previous *Chandra* and *XMM-Newton* observations. The spectral variation in *F05189–2524* suggests that the central source may have turned off, leaving behind a residual reflection component. However, an increase in column density cannot be completely ruled out. The absorption-corrected 2–10 keV luminosity to infrared luminosity ratios of *F05189–2524* during its “high” state is consistent with values observed in PG quasars.
2. The XIS spectrum of Mrk 273 contains a strong Fe  $K\alpha$  line and shows a change in the observed 2–10 keV spectrum relative to previous *Chandra* and *XMM-Newton* observations. Mrk 273 is marginally ( $1.8\text{-}\sigma$ ) detected at high energies, with the HXD/PIN spectrum  $\sim 5.4\%$  above the background. A change in the covering fraction of the absorber best explains the spectral variations in Mrk 273, although a drop in the intrinsic AGN luminosity cannot be formally ruled out. A column density of  $\sim 10^{24} \text{ cm}^{-2}$  is derived from the *Suzaku* data. The changes in spectral shape and covering fraction on a time scale of a few years suggest that the absorbing matter is  $\sim 1 \text{ pc}$  from the central source. The Mrk 273 spectrum is best modeled by a  $\sim 94\%$  covering fraction model. The absorption-corrected 2–10 keV luminosity to infrared luminosity ratios of Mrk 273 is consistent with values observed in PG quasars.
3. *F08572+3915* is undetected in the *Suzaku* XIS and HXD/PIN observations. The low X-ray count rate derived from unpublished *Chandra* observations, combined with mid-infrared observations, suggests that this source is highly obscured.

4. PKS 1345+12 is detected by the XIS. No apparent flux or spectral variability is detected in its 0.5–10 keV spectrum relative to previous *Chandra* observations. The net 15–40 keV HXD/PIN spectrum is only  $1.1\sigma$  above the total background, not strong enough for a meaningful full-band (XIS+HXD/PIN) spectral fitting. Unlike other ULIRGs, the 0.5–2 keV spectrum of this source does not contain an obvious thermal MEKAL component. Combining this result and the fact that the absorption-corrected 2–10 keV to infrared luminosity ratio of PKS 1345+12 is in agreement with those of PG quasars, the data suggest that the X-ray luminosity of this object is dominated by an AGN.
5. Arp 220 is detected by the XIS, but not by the HXD/PIN. Its 0.5–10 keV spectrum, including the iron complex, appears unchanged since previous *Chandra* observations. The X-ray continuum emission is in agreement with the possibility that a highly obscured AGN is present. This interpretation of the data is consistent with previous CO observations. The measurements of the iron emission line at 6.7 keV can be reconciled by the ionized reflection model.
6. In all three cases where an optically thin thermal component is contributing to the soft X-ray emission detected by XIS (*F*05189–2524, Mrk 273, Arp 220), the temperature,  $kT \sim 0.3\text{--}0.8$  keV, is consistent with previous observations of ULIRGs.

We are grateful to the anonymous referee for providing very useful comments and suggestions that have greatly improved this paper. We would like to acknowledge Dr. Coleman Miller for useful discussions. We are also grateful for the extensive help on data reduction provided by the NASA/HEASARC *Suzaku* GOF team. The data reduction for this paper made use of a module in the Beowulf cluster (“the Borg”) in the Department of Astronomy, University of Maryland. This research also utilized the NASA/IPAC Extragalactic Database (NED), which is operated by the Jet Propulsion Laboratory, Caltech, under contract with NASA. We acknowledge support from the NASA/*Suzaku* Guest Observer Program under grant NNX06AI39G. This research has made use of data obtained from the *Suzaku* satellite, a collaborative mission between the space agencies of Japan (JAXA) and the USA (NASA).

## REFERENCES

- Armus, L. et al. 2007, ApJ, 656 148
- Balestra, I., Boller, Th., Gallo, L., Lutz, D., & Hess, S. 2005, A&A, 442, 469

- Clements, D.L., McDowell, J.C., Shaked, S., Baker, A.C., Borne, K., Colina, L., Lamb, S.A., & Mundell, C. 2002, *ApJ*, 581, 974
- Dermer, C.D., Bland-Hawthorn, J., Chiang, J., & McNaron-Brown, K. 1997, *ApJ*, 484, L121
- Dickey & Lockman 1990, *ARAA*, 28, 215
- Downes, D. & Eckart, A. 2007, *A&A*, 468, L57
- Downes, D., & Solomon, P. M. 1998, *ApJ*, 507, 615
- Ebisawa, K., Bourban, G., Bodaghee, A., Mowlavin, N., & Courvoisier, T.J.-L. 2003, *A&A*, 411, L49
- Elvis, M., Wilkes, B.J., McDowell, J.C., Green, R.G., Bechtold, J., Willner, S.P. Oey, M.S., Polomski, E., & Cutri, R. 1994, *ApJS*, 95, 1
- Evans, A.S., Kim, D. C., Mazzarella, J. M., Scoville, N. Z., & Sanders, D. B., 1999, *ApJ*, 521, L107
- Evans, A.S., Mazzarella, J.M., Surace, J.A., & Sanders, D.B. 2002, *ApJ*, 580, 749
- Franceschini, A., Braito, V., Persic, M., Della Ceca, R., Bassani, L., Cappi, M., Malaguti, P., Palumbo, G.G.C., Risaliti, G., Salvati, M., & Severgnini, P. 2003, *MNRAS*, 343, 1181
- Grimes, J.P., Heckman, T., Strickland, D., & Ptak, A., 2005, *ApJ*, 628, 187
- Guainazzi et al., 1998, *ApJ*, 301, L1
- Imanishi, M. & Terashima, Y. 2004, *ApJ*, 127, 758
- Imanishi, M., Dudley, C.C., & Maloney, P.R. 2006, *ApJ*, 637, 114
- Iwasawa, K. 1999, *MNRAS*, 302, 96
- Iwasawa, K., Matt, G., Guainazzi, M., & Fabian, A.C. 2001, *MNRAS*, 326, 894
- Iwasawa, K., Sanders, D.B., Evans, A.S., Trentham, N., Miniutti, G., & Spoon, H.W.W. 2005, *MNRAS*, 357, 565
- Kim, D.-C., Veilleux, Sylvain, & Sanders, D.B. 1998, *ApJ*, 508, 627
- Lonsdale, C.J., Smith, H.J., & Lonsdale, C.J. 1993, *ApJ*, 405, L9

- Matt, G., Pompilio, F., & La Franca, F., 1999, *New Astronomy*, 4, 191
- McDowell, J.C., Clements, D.L., Lamb, S.A., Shaked, S., Hearn, N.C., Colina, L., Mundell, C., Borne, K., Baker, A.C., & Arribas, S. 2003, *ApJ*, 591, 164
- Nagar, N.M., Wilson, A.S., Falcke, H., Veilleux, S., & Maiolino, R., 2003, *A&A*, 409, 115
- Piconcelli, E., Jimenez-Bailon, E., Guainazzi, M., Schartel, N., Rodriguez-Pascual, P.M. & Santos-Lleo, M., 2005, *A&A*, 432, 15
- Polletta, M., Bassani, L., Malaguti, G., Palumbo, G.G.C., & Caroli, E. 1996, *ApJS*, 106, 399
- Ptak, A., Heckman, T., Levenson, N.A., Weaver, K., & Strickland, D. 2003, *ApJ*, 592, 782
- Risaliti, G., Gilli, R., Maiolino, R., & Salvati, M. 2000, *A&A*, 357, 13
- Risaliti, G., Elvis, M., Fabbiano, G., Baldi, A., & Zezas, A., 2005, *ApJ*, 623, L93
- Ross, R.R. & Fabian, A.C. 2005, *MNRAS*, 358, 211
- Rupke, D. S. N., Veilleux, S., & Baker, A. J. 2008, *ApJ*, 674, 172
- Sanders, D.B., & Mirabel, I. N. 1996, *ARA&A*, 34, 749
- Sanders, D.B., Soifer, B. T., Elias, J. H., Madore, B. F., Matthews, K., Neugebauer, G., & Scoville, N. Z. 1988, *ApJ*, 325, 74
- Sanders, D.B., Mazzarella, J.M., Kim, D.-C., Surace, J.A., & Soifer, B.T. 2003, *AJ*, 126, 1607
- Severgnini, P., Risaliti, G., Marconi, A., Maiolino, R., & Salvati, M. 2001, *A&A*, 368, 44
- Teng, S.H., Wilson, A.S., Veilleux, S., Young, A.J., Sanders, D.B., & Nagar, N.M. 2005, *ApJ*, 633, 664
- Teng, S.H., Veilleux, S., Wilson, A.S. Young, A.J., Sanders, D.B., & Nagar, N.M., 2008, *ApJ*, 674, 133
- Terashima, Y. & Wilson, A.S. 2003, *AJ*, 583, 145
- Turner, T.J. & Pounds, K.A. 1989, *MNRAS*, 240, 833
- Veilleux, Sylvain, Sanders, D.B., & Kim, D.-C., 1997, *ApJ*, 484, 92
- Veilleux, S., Kim, D.-C., & Sanders, D.B. 1999a, *ApJ*, 522, 113

Veilleux, S., Sanders, D.B., & Kim, D.-C. 1999b, ApJ, 522, 139

Veilleux, S., Kim, D.-C., & Sanders, D.B. 2002, ApJS, 143, 315

Veilleux, S. et al., 2006, ApJ, 643, 707

Veilleux, S. et al., 2008, ApJ, submitted.

Xia, X.Y., Boller, Th., Wu, H., Deng, Z.G., Gao, Y., Zou, Z.L., Mao, S., & Borner, G. 1998,  
ApJ, 496, L9(erratum 507, L99)

Xia, X.Y., Xue, S.J., Mao, S., Boller, Th., Deng, Z.G., & Wu, H. 2002, ApJ, 564, 196



Table 1. The Sample

Object	$z$	$\log F_{\text{IR}}$ [ergs/s/cm <sup>2</sup> ]	$f_{25\ \mu\text{m}}/f_{60\ \mu\text{m}}$	Spectral Type	$N_{\text{H,Galactic}}$ [10 <sup>20</sup> cm <sup>-2</sup> ]	Scale [kpc/'']	$D_{\text{L}}$ [Mpc]
(1)	(2)	(3)	(4)	(5)	(6)	(7)	(8)
F05189–2524	0.042	–8.87	0.25	S2/S1	1.92	0.71	173.3
F08572+3915	0.058	–9.18	0.23	LINER/S2	2.60	1.05	242.0
Mrk 273	0.038	–8.78	0.10	S2	1.10	0.70	156.3
PKS 1345+12	0.122	–9.65	0.35	S2/S1	1.90	2.05	531.8
Arp 220	0.018	–8.11	0.08	LINER	4.27	0.34	72.9

Note. — Col. (1): Object name. Col (2): redshift. Col. (3): logarithm of infrared (8–1000  $\mu\text{m}$ ) flux. Col. (4): the 25-to-60  $\mu\text{m}$  *IRAS* flux ratio, a measure of the dust temperature. Col. (5): galaxy spectral type. Col. (6): Galactic hydrogen column density (Dickey & Lockman 1990). Col. (7): Physical size corresponding to 1''. Col. (8): Luminosity distance.

Table 2. *Suzaku* Observations

Object	Observation ID	PI Name	Date [UT]	XIS Net Exposure [ksec]	HXD Net Exposure [ksec]
(1)	(2)	(3)	(4)	(5)	(6)
F05189–2524	701097010	Veilleux; Anabuki	2006 April 10	78.2	48.0
F08572+3915	701053010	Gallagher	2006 April 14	77.2	58.1
Mrk 273	701050010	Veilleux	2006 July 7	79.9	76.3
PKS 1345+12	702053010	Veilleux	2008 January 7	53.0	41.4
Arp 220	700006010	<i>Suzaku</i> SWG	2006 January 7	98.6	86.9

Note. — Col. (1): Object name. Col (2)–(3): *Suzaku* proposal number and principal investigator of archived data. Col. (4): beginning observing date in UT. Col. (5)–(6): net exposure time in kiloseconds after screening and HXD deadtime corrections.

Table 3. Best-fit Parameters to *Suzaku* Spectra<sup>†</sup>

Object	Best-fit Model	kT [keV]	$\Gamma$	$N_{\text{H, source}}$ [ $10^{23} \text{ cm}^{-2}$ ]	$f$	$E_{\text{line}}$ [keV]	$\sigma$ [keV]	EW [keV]	$K$	$\chi^2/\text{d.o.f.}$	Observed $F_{0.5-2 \text{ keV}}$	Unabsorbed $F_{0.5-2 \text{ keV}}$	Observed $F_{2-10 \text{ keV}}$	Unabsorbed $F_{2-10 \text{ keV}}$	Observed $F_{12-40 \text{ keV}}$	Unabsorbed $F_{12-40 \text{ keV}}$
(1)	(2)	(3)	(4)	(5)	(6)	(7)	(8)	(9)	(10)	(11)	(12)	(13)	(14)	(15)	(16)	(17)
XIS Only																
F05189-2524	A	$0.71^{+0.13}_{-0.08}$	$2.68^{+0.30}_{-0.13}$	—	82.73	$6.40^{+0.14}_{-0.87}$	$0.00^{+0.82}_{-0.00}$	$0.47^{+0.75}_{-0.41}$	$2.20^{+0.48}_{-0.74} \times 10^{-5}$	185/123	$0.66^{+0.10}_{-0.10}$	$0.70^{+0.14}_{-0.10}$	$1.03^{+0.39}_{-0.38}$	$1.03^{+0.40}_{-0.40}$	—	—
Mrk 273	B	$0.64^{+0.04}_{-0.04}$	$1.56^{+0.15}_{-0.09}$	$8.64^{+1.71}_{-1.20}$	0.09	$6.39^{+0.03}_{-0.03}$	$0.00^{+0.10}_{-0.00}$	$0.56^{+0.15}_{-0.11}$	$3.65^{+1.84}_{-0.90} \times 10^{-4}$	233/187	$1.17^{+0.10}_{-0.13}$	$8.98^{+4.10}_{-2.05}$	$4.29^{+0.13}_{-1.67}$	$20.44^{+9.48}_{-4.84}$	—	—
PKS 1345+12	B	—	$1.64^{+0.09}_{-0.11}$	$0.43^{+0.03}_{-0.07}$	0.02	—	—	—	$3.13^{+0.52}_{-0.64} \times 10^{-4}$	164/156	$0.37^{+0.09}_{-0.09}$	$5.93^{+2.47}_{-3.73}$	$9.53^{+3.17}_{-4.06}$	$11.91^{+3.12}_{-4.64}$	—	—
Arp 220	C	$0.67^{+0.07}_{-0.04}$	$1.93^{+0.04}_{-0.07}$	$0.07^{+0.02}_{-0.02}$	—	$6.70^{+0.13}_{-0.08}$	$0.05^{+0.27}_{-0.05}$	$0.42^{+0.54}_{-0.32}$	$1.80^{+0.78}_{-0.40} \times 10^{-9} \ddagger$	181/176	$0.66^{+0.10}_{-0.11}$	$1.85^{+0.75}_{-0.40}$	$0.98^{+0.24}_{-0.42}$	$1.04^{+0.72}_{-0.35}$	—	—
Combined XIS+HXD/PIN Spectra																
Mrk 273	B	$0.64^{+0.04}_{-0.04}$	$1.40^{+0.10}_{-0.11}$	$14.09^{+1.63}_{-1.53}$	0.05	$6.38^{+0.03}_{-0.04}$	$0.03^{+0.08}_{-0.03}$	$0.68^{+0.18}_{-0.15}$	$6.14^{+2.39}_{-1.77} \times 10^{-4}$	268/199	$1.15^{+0.12}_{-0.10}$	$14.50^{+5.32}_{-3.98}$	$4.68^{+0.75}_{-1.53}$	$43.19^{+16.03}_{-12.09}$	$66.59^{+22.43}_{-35.53}$	$76.27^{+28.79}_{-21.45}$

Note. — <sup>†</sup> F08572+3915 is undetected by the XIS and is thus not included in this table. <sup>‡</sup> Since the spectrum is pure reflection, the normalization factor is of the reflection component. Col. (1): Object name. Col. (2): favored model – (A) reflection plus power law model, (B) scattering model, (C) ionized reflection model. Col (3): temperature of the thermal starburst component from the MEKAL model. Col. (4): slope to the power-law model. Col. (5): absorption within the source. Col. (6): the ratio of the normalization parameter between the reflected (or scattered) component to the direct component. Col. (7): rest energy of the emission line. Col. (8): line width of the emission line. Col. (9): equivalent width of the emission line. Col. (10): normalization factor of the reflect component in photons  $\text{cm}^{-2} \text{ s}^{-1}$  at 1 keV. Col. (11):  $\chi^2$  fitting statistics per degree of freedom. Col. (12)–(17): flux in units of  $10^{-13} \text{ ergs s}^{-1} \text{ cm}^{-2}$ .

Table 4. Best-fit Parameters to Spectra of F05189–2524 and Mrk 273 from Multiple Epochs

Telescope	kT	$\Gamma$	$f$	$N_{\text{H}, \text{source } 1}$	$f_{\text{cover } 1}$	$N_{\text{H}, \text{source } 2}$	$f_{\text{cover } 2}$	$E_{\text{line}}$	$\sigma$	EW	$K$	Observed	Unabsorbed	Observed	Unabsorbed	Observed	Unabsorbed
(1)	[keV]	(3)	(4)	[ $10^{23} \text{ cm}^{-2}$ ]	(6)	[ $10^{23} \text{ cm}^{-2}$ ]	(8)	[keV]	[keV]	[keV]	(12)	$F_{0.5-2 \text{ keV}}$	$F_{0.5-2 \text{ keV}}$	$F_{2-10 \text{ keV}}$	$F_{2-10 \text{ keV}}$	$F_{15-40 \text{ keV}}$	$F_{15-40 \text{ keV}}$
F05189–2524: scattering model, change in column density ( $\chi^2/\text{d.o.f.} = 640/503$ )																	
XMM (2001)	$0.23^{+0.02}_{-0.03}$	$1.91^{+0.08}_{-0.05}$	0.02	$0.58^{+0.03}_{-0.03}$	—	—	—	$6.37^{+0.27}_{-0.25}$	$0.73^{+0.31}_{-0.16}$	$0.64^{+0.98}_{-0.63}$	$1.42^{+0.17}_{-0.12} \times 10^{-3}$	$1.02^{+0.10}_{-0.11}$	$30.00^{+1.29}_{-17.53}$	$29.38^{+5.42}_{-4.35}$	$42.03^{+6.58}_{-1.79}$	—	—
Chandra (2001)	0.23	1.91	0.02	$0.90^{+0.05}_{-0.05}$	—	—	—	6.37	0.73	0.64	$1.42 \times 10^{-3}$	$0.77^{+0.08}_{-0.08}$	30.00	$25.67^{+3.33}_{-5.79}$	42.03	—	—
Chandra (2002)	0.23	1.91	0.02	$0.71^{+0.04}_{-0.03}$	—	—	—	6.37	0.73	0.64	$1.42 \times 10^{-3}$	$0.87^{+0.09}_{-0.09}$	30.00	$27.69^{+3.66}_{-7.16}$	42.03	—	—
Suzaku (2006)	0.23	1.91	0.02	$21.55^{+2.18}_{-1.71}$	—	—	—	6.37	0.73	0.64	$1.42 \times 10^{-3}$	$0.70^{+0.10}_{-0.08}$	30.00	$1.45^{+0.28}_{-0.25}$	42.03	—	—
F05189–2524: reflection dominated, change in AGN luminosity ( $\chi^2/\text{d.o.f.} = 659/502$ )																	
XMM (2001)	$0.24^{+0.02}_{-0.01}$	$1.79^{+0.07}_{-0.13}$	0.02	$0.59^{+0.05}_{-0.05}$	—	—	—	—	—	—	$1.27^{+0.24}_{-0.21} \times 10^{-3}$	$1.02^{+0.12}_{-0.10}$	$27.02^{+1.55}_{-18.21}$	$29.92^{+3.15}_{-4.03}$	$42.80^{+6.03}_{-0.50}$	—	—
Chandra (2001)	0.24	1.79	0.02	$0.93^{+0.09}_{-0.09}$	—	—	—	—	—	—	$1.27 \times 10^{-3}$	$0.77^{+0.10}_{-0.11}$	27.02	$25.90^{+2.72}_{-3.03}$	42.80	—	—
Chandra (2002)	0.24	1.79	0.02	$0.72^{+0.07}_{-0.06}$	—	—	—	—	—	—	$1.27 \times 10^{-3}$	$0.87^{+0.10}_{-0.10}$	27.02	$28.16^{+3.14}_{-3.82}$	42.80	—	—
Suzaku (2006)	0.24	1.79	6.82	—	—	—	—	$6.32^{+0.17}_{-0.22}$	$0.00^{+0.46}_{-0.00}$	$1.95^{+3.64}_{-1.00}$	$2.18^{+0.30}_{-0.36} \times 10^{-5}$	$0.69^{+0.09}_{-0.10}$	$0.75^{+0.10}_{-0.10}$	$1.06^{+0.33}_{-0.14}$	$1.06^{+0.36}_{-0.11}$	—	—
Mrk 273: change in covering fraction ( $\chi^2/\text{d.o.f.} = 521/376$ )																	
Chandra (2000)	$0.79^{+0.03}_{-0.03}$	$1.73^{+0.04}_{-0.02}$	—	$15.91^{+0.86}_{-0.73}$	$0.80^{+0.01}_{-0.02}$	$3.00^{+0.23}_{-0.20}$	$0.96^{+0.01}_{-0.01}$	$6.40^{+0.01}_{-0.13}$	$0.00^{+0.06}_{-0.00}$	$0.25^{+0.04}_{-0.07}$	$2.24^{+0.20}_{-0.11} \times 10^{-3}$	$0.73^{+2.92}_{-0.15}$	$47.29^{+4.25}_{-2.26}$	$7.49^{+3.06}_{-2.36}$	$84.10^{+7.89}_{-4.48}$	—	—
XMM(2002)	0.79	1.73	—	15.91	$0.94^{+0.01}_{-0.01}$	3.00	$0.81^{+0.02}_{-0.02}$	6.40	0.00	0.25	$2.24 \times 10^{-3}$	$0.85^{+0.05}_{-0.27}$	47.29	$4.09^{+0.55}_{-1.87}$	84.10	—	—
Suzaku(2006)	0.79	1.73	—	15.91	$0.94^{+0.01}_{-0.01}$	3.00	$0.69^{+0.02}_{-0.02}$	6.40	0.00	0.25	$2.24 \times 10^{-3}$	$1.11^{+0.03}_{-0.42}$	47.29	$4.36^{+0.30}_{-1.96}$	84.10	$67.35^{+22.51}_{-40.50}$	$78.48^{+8.40}_{-4.45}$

Note. — Col. (1): Spacecraft used and year of the observation. Col (2): temperature of the thermal starburst component from the MEKAL model. Col. (3): slope to the power-law model. Col. (4): the ratio of the normalization parameters between the reflected (or scattered) component to the direct component. Col. (5)–(8): absorption within the source and corresponding covering fraction for the covering fraction absorber model. Col. (9): rest energy of the emission line. Col. (10): line width of the emission line. Col. (11): equivalent width of the emission line. Col. (12): normalization factor of the direct component in photons  $\text{cm}^{-2} \text{ s}^{-1}$ . Col. (13)–(18): flux in units of  $10^{-13} \text{ ergs s}^{-1} \text{ cm}^{-2}$ .

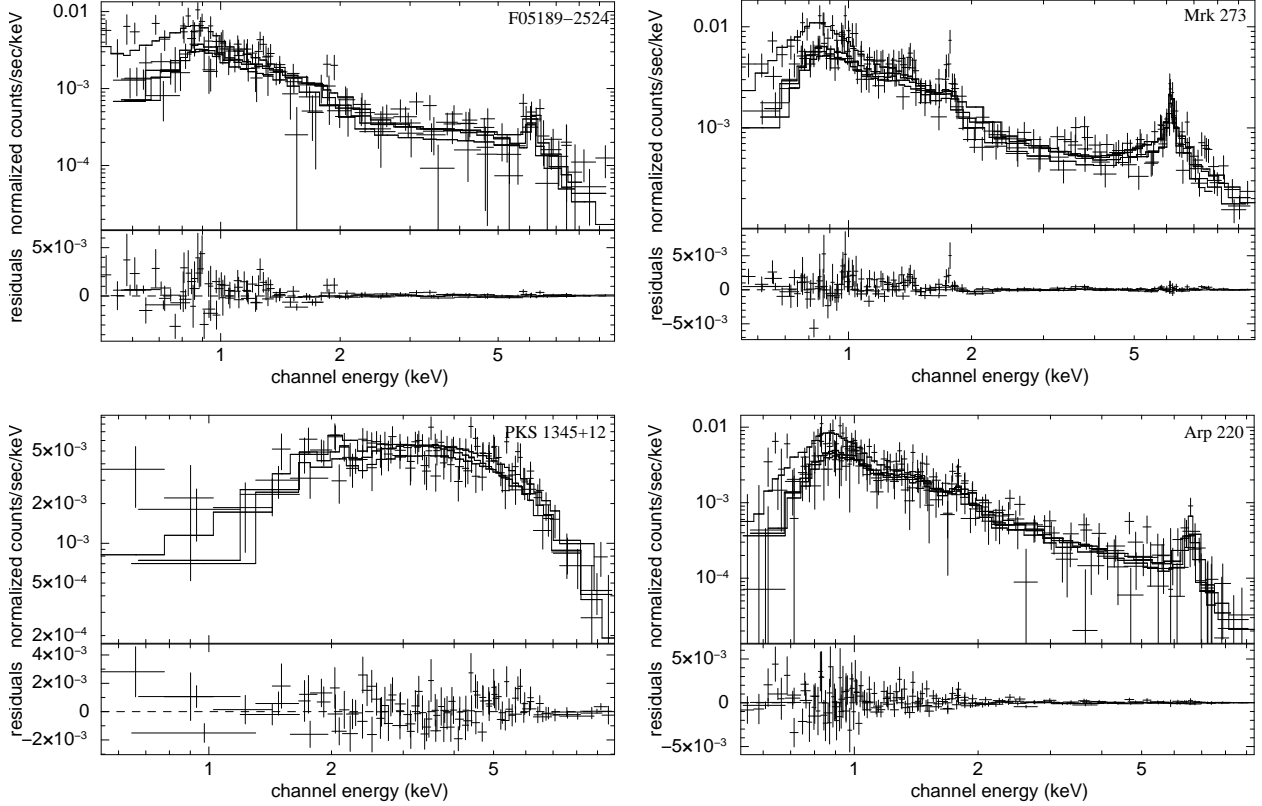


Fig. 1.— Spectra of *F05189–2524* (top left), *Mrk 273* (top right), *PKS 1345+12* (bottom left) and *Arp 220* (bottom right) with their respective best-fit models for all four XIS detectors. *F08572 + 3915* is not detected by the XIS. The data are binned to at least 50 counts bin<sup>-1</sup> for *PKS 1345+12* and at least 15 counts bin<sup>-1</sup> for the others. The horizontal axis is energy in the observer’s frame. In *F05189–2524*, *Mrk 273*, and *Arp 220*, an emission line is detected near 6.4–6.7 keV, consistent with emission arising from neutral or ionized iron. The same emission line also appears to be present in *PKS 1345+12*, but the detection is not statistically significant ( $\Delta\chi^2=2.0$  for  $\Delta\text{d.o.f}=2$ ). Other than *PKS 1345+12*, the 0.5–2 keV spectrum for each object has a thermal component with temperatures of  $\sim 0.7\text{--}0.8$  keV, consistent with earlier results on ULIRGs. The best-fit parameters are listed in Table 3.

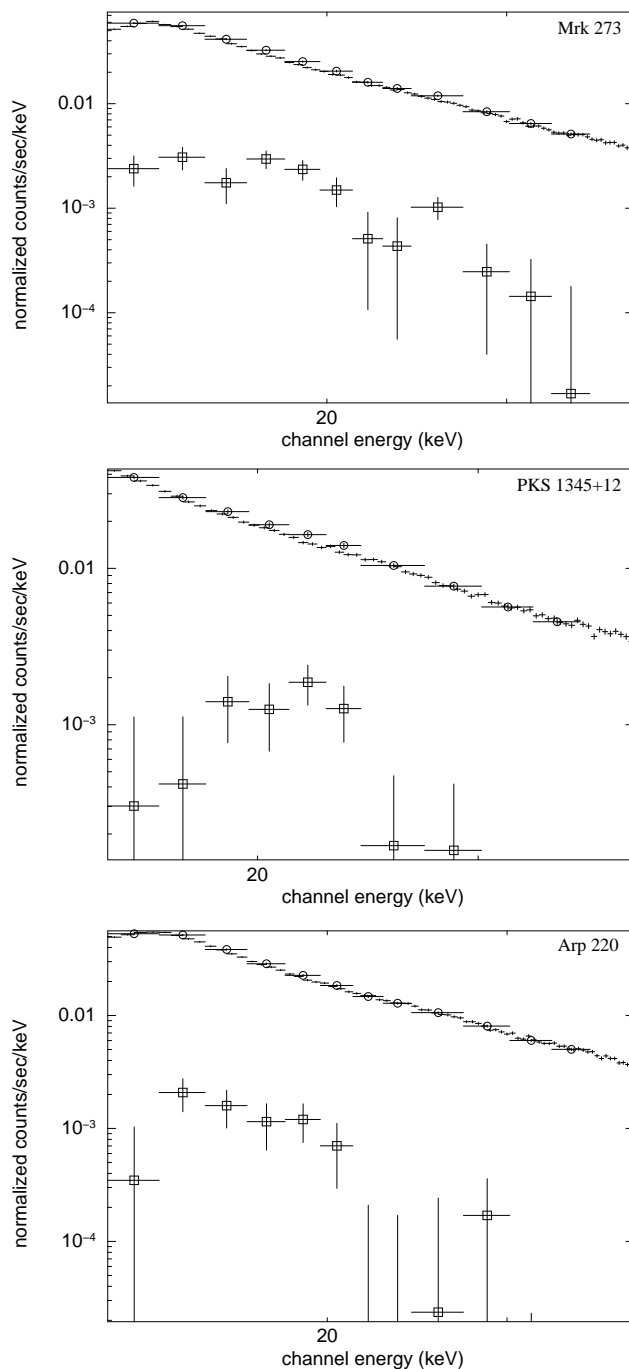


Fig. 2.— HXD/PIN spectrum (open circles), together with the background spectrum (NXB+CXB; small crosses) and the net spectrum (open squares) of Mrk 273, PKS 1345+12, and Arp 220. The net spectrum for Mrk 273, PKS 1345+12, and Arp 220 is 5.4%, 3.4%, and 2.2% above the background, respectively. Mrk 273 is the only source that is detected above the background beyond the uncertainties of the background modeling (at the  $1.8\text{-}\sigma$  level). The spectra of *F05189–2524* and *F08572+3915* do not lie above the background, so they are not shown here.

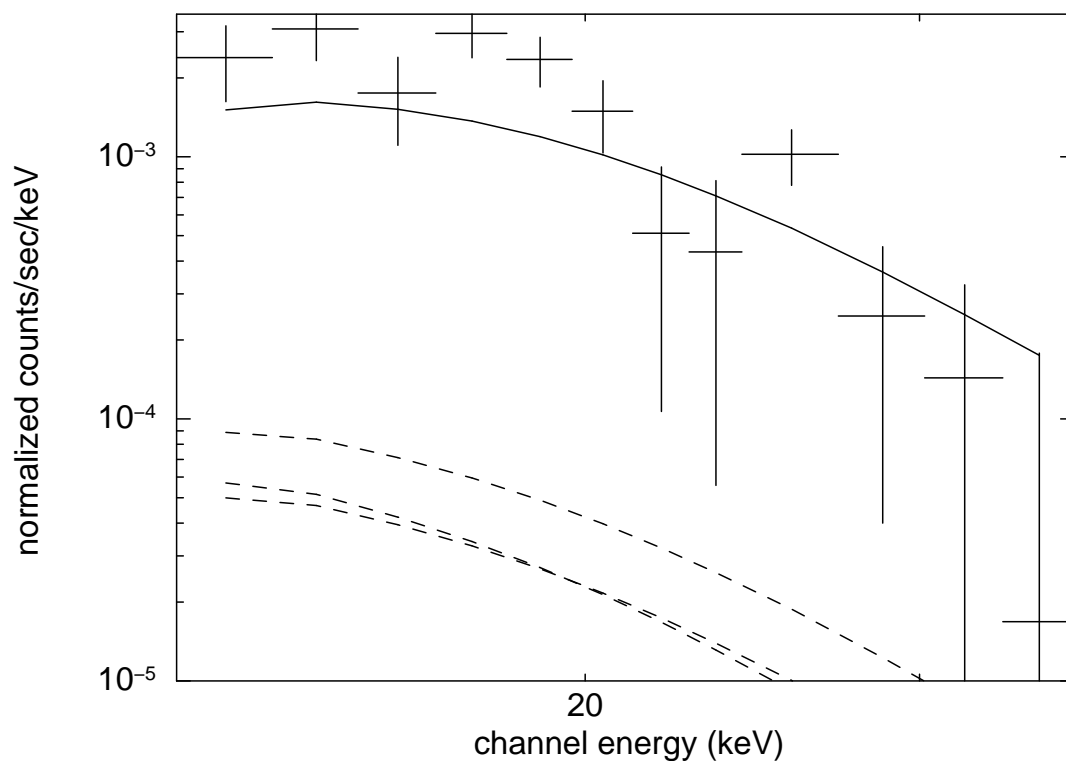


Fig. 3.— The net background-subtracted 15–40 keV HXD/PIN spectrum of Mrk 273 compared with the spectral models of possible contaminants in the PIN field of view. The solid line represents the best-fit model from the XIS-HXD/PIN spectral fitting and is a sum of the flux from Mrk 273 and the contaminants. The dashed lines represent the best-fit XIS models of the contaminants extrapolated to the HXD/PIN energy range. The contributions from these contaminants to the overall PIN signals are negligible.

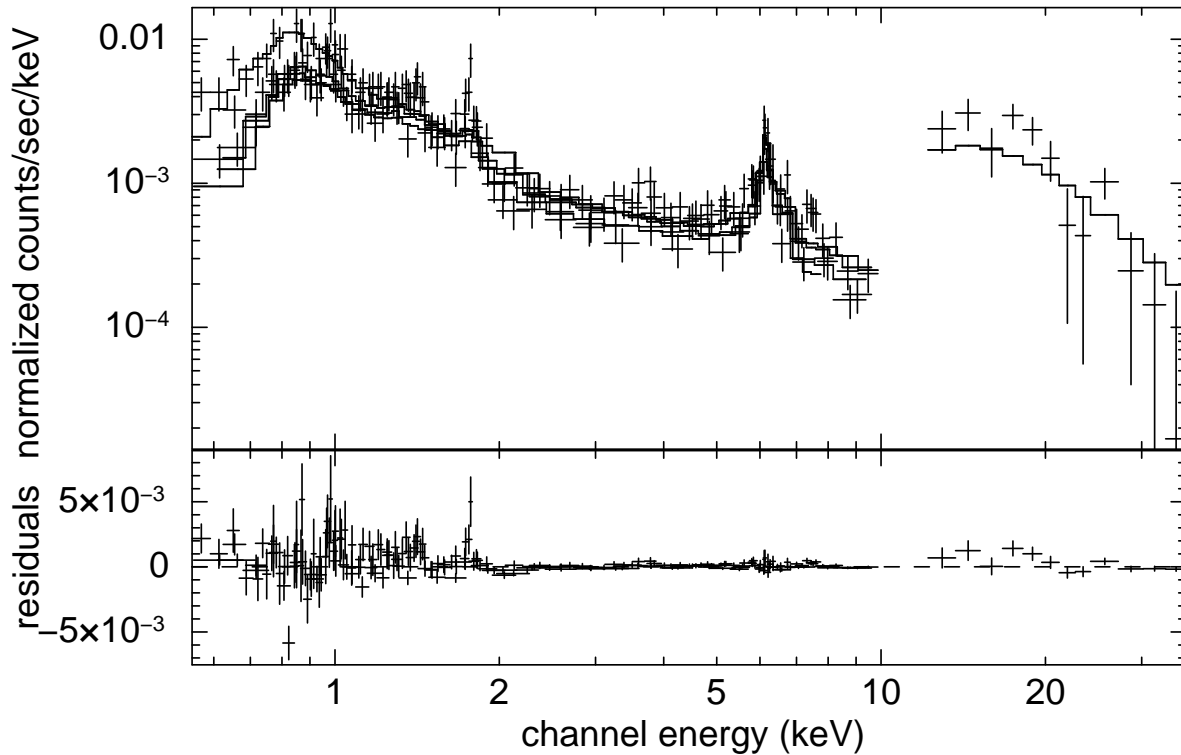


Fig. 4.— The combined XIS-HXD/PIN spectrum of Mrk 273 with the best-fit scattering model. The horizontal axis is energy in the observer’s frame. The directly transmitted AGN flux is  $\sim 5\%$  of the intrinsic flux. The iron line at  $\sim 6.4$  keV is detected and a MEKAL model with gas temperature  $\sim 0.7$  keV is needed to reproduce the soft X-rays. The cross-normalization of the HXD/PIN with respect to XIS0 is assumed to be 1.13. The best-fit parameters for the full band (XIS+HXD/PIN) modeling are listed in Table 3.

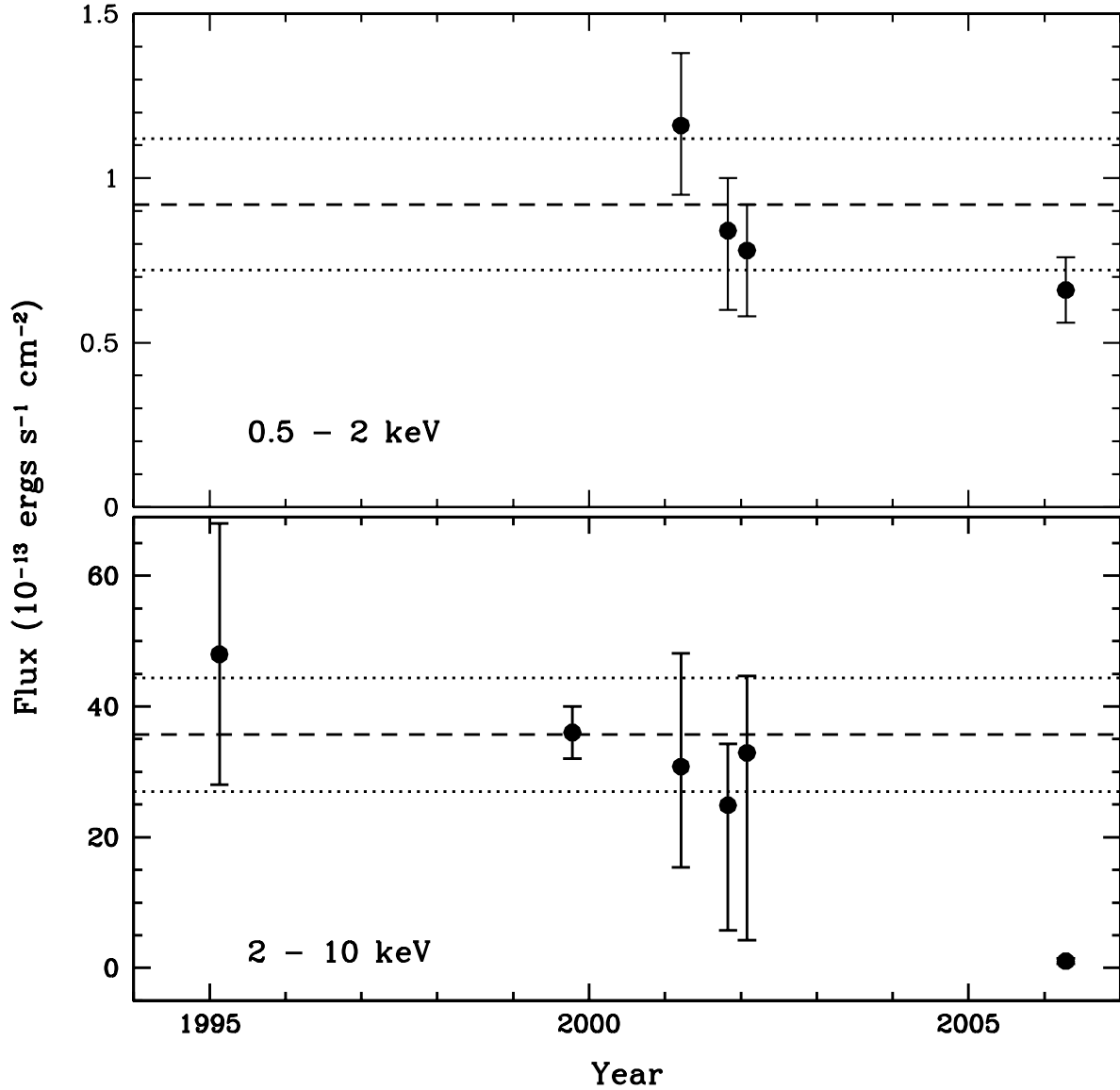


Fig. 5.— Observed 0.5–2 keV (top) and 2–10 keV (bottom) fluxes of *F05189–2524* from 1995 to 2006 as determined from *ASCA*, *BeppoSAX*, *XMM-Newton*, *Chandra*, and *Suzaku* data. While there has been little change in the 0.5–2 keV flux, the nominal 2–10 keV flux of *F05189–2524* has decreased by a factor of  $\sim 30$  since previous observations. The dashed line represents the average “high” state flux (measurements made prior to *Suzaku*) as weighted by the measurement errors while the dotted lines denote one standard deviation away from the mean. The 2–10 keV flux value as measured by *Suzaku* is  $\sim 4$  standard deviations away from the weighted mean. The *ASCA* (1995) and *BeppoSAX* (1999) values are drawn from Severgnini et al. (2001); the *XMM-Newton* (2001) and *Chandra* (2002) values are drawn from our modeling of the archived spectra with the scattering model in this work (see §5.1). The error bars for the 2006 value are within the data point.



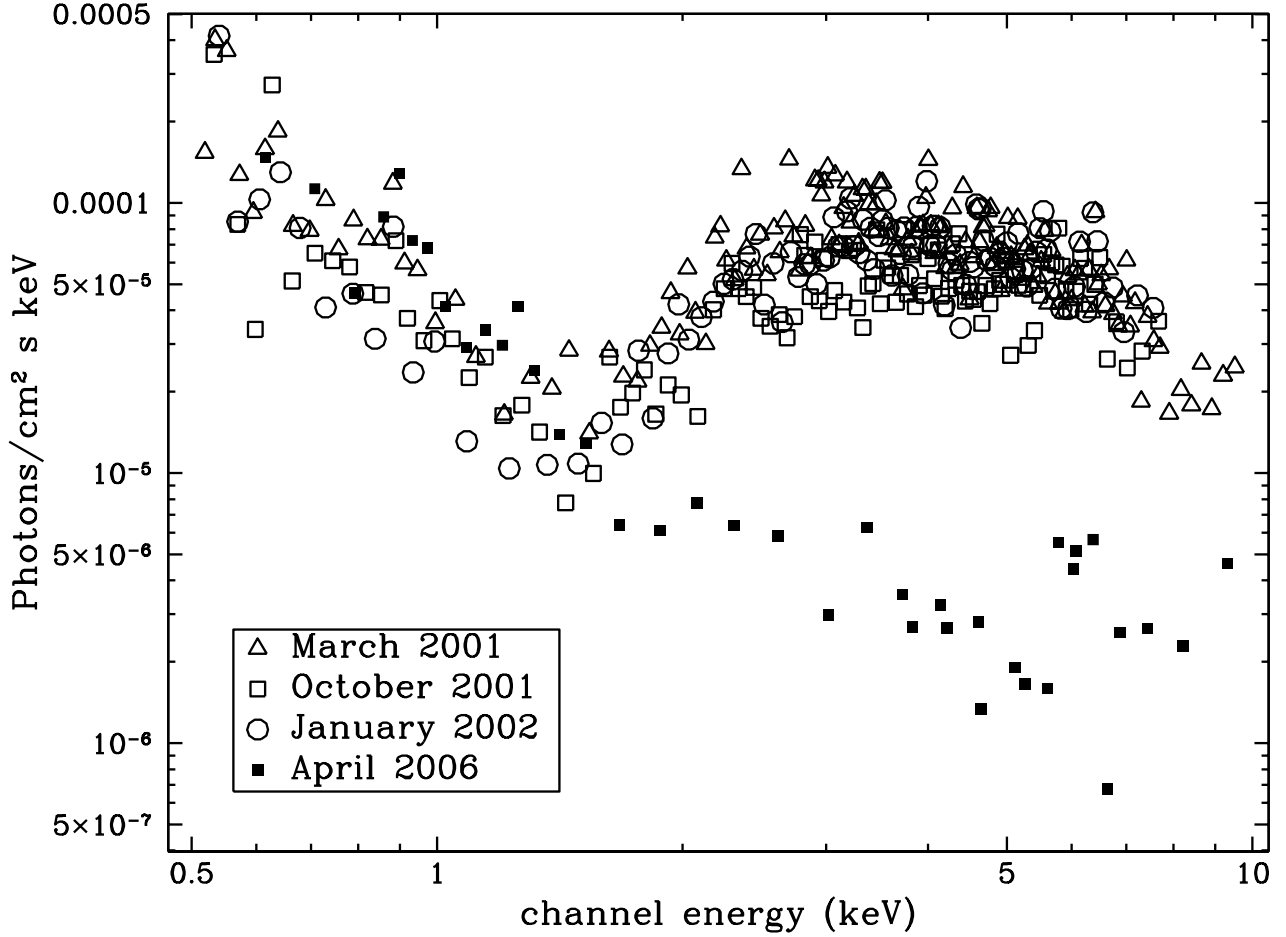


Fig. 6.— Comparison of the unfolded spectra of *F05189–2524* from the 2001 March *XMM-Newton* (open triangles), 2001 October *Chandra* (open squares), 2002 January *Chandra* (open circles), and 2006 April *Suzaku* (closed squares) observations. The unfolded spectra were created using the best-fit models to each individual spectrum. Below  $\sim 1.3$  keV, there appears to have been negligible change in flux or spectral shape between the different observations. However, above  $\sim 1.3$  keV, the spectral change is obvious. The iron line is prominent in the *Suzaku* data, but is not noticeable in the other observations. The best-fit models to the spectrum changed from a scattering-dominated scenario in 2001 and 2002 to a reflection-dominated scenario in 2006. This may be an indication that the central source has faded prior to 2006 or variations in the column density.

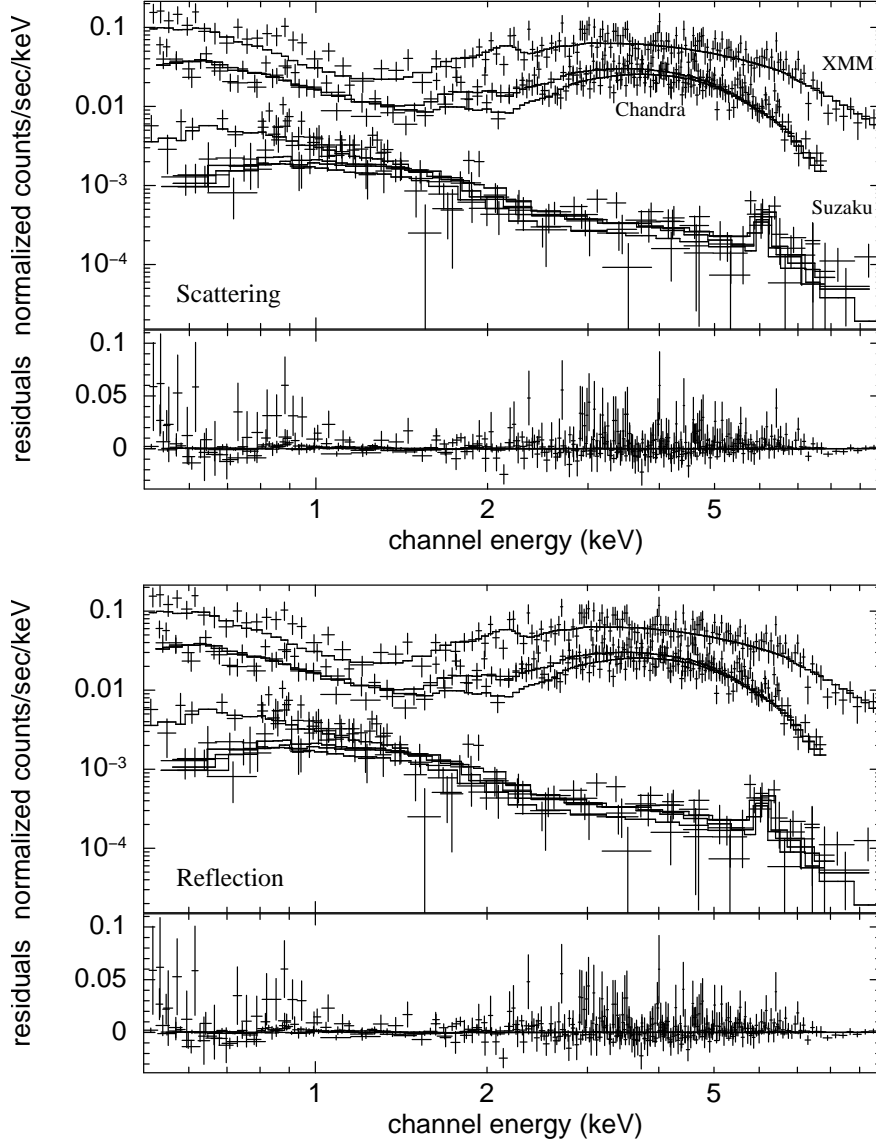


Fig. 7.— The two models to the *Chandra*-ACIS, *XMM-Newton*-EPIC pn, and *Suzaku*-XIS/PIN data used to explain the change in the 2–10 keV spectral shape of *F05189–2524*: (top) change in the absorbing column alters the spectral shape of the source, and (bottom) the AGN has switched off and has left behind a residual reflection component (see §5.1 for details). The response from each detector is folded in with the data. The horizontal axis is energy in the observer’s frame. The cross-normalization factor is assumed to be unity for *XMM-Newton* and *Chandra* with respect to *Suzaku*-XIS0. Both models have comparable reduced  $\chi^2$  values (1.27 for 503 d.o.f. versus 1.30 for 502 d.o.f.) and appear to fit the overall 0.5–10 keV spectrum well. Neither model can be ruled out by the data. Table 4 lists the results from this modeling.

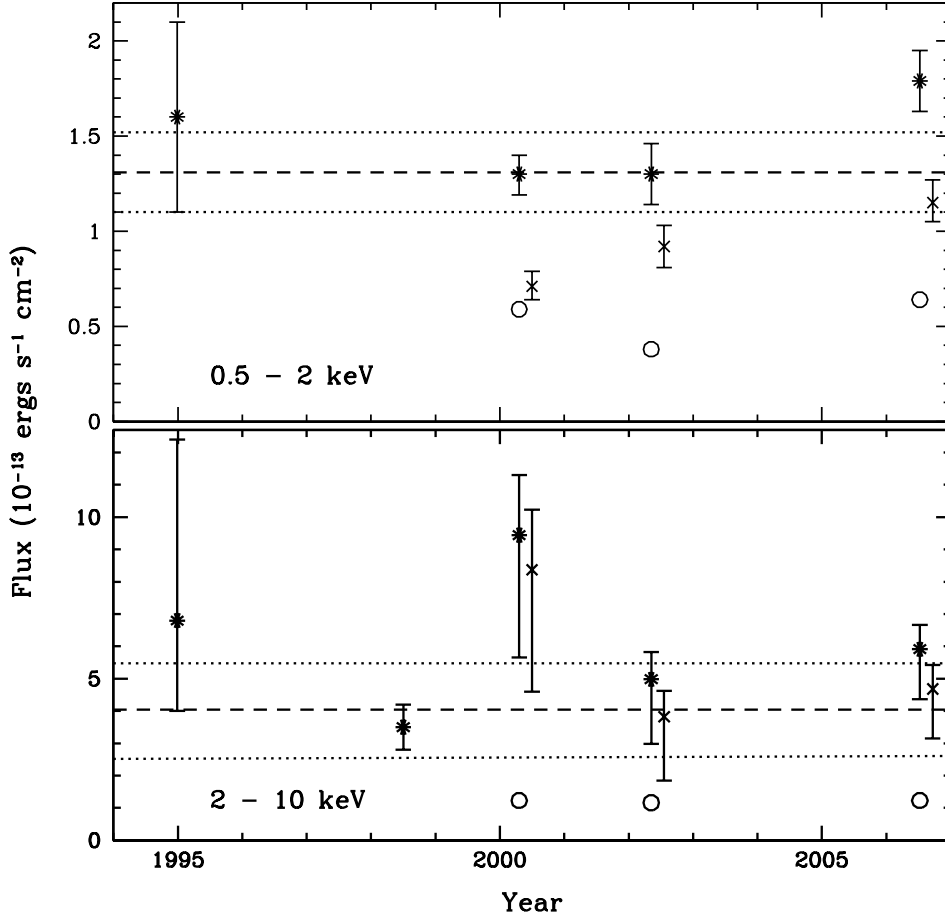


Fig. 8.— Observed 0.5–2 keV (top) and 2–10 keV (bottom) fluxes of Mrk 273 (crosses) and Mrk 273x (open circles) from 1994 to 2006 as determined from *ASCA*, *BeppoSAX*, *XMM-Newton*, *Chandra*, and *Suzaku* data. Each asterisk represents the sum of the fluxes from Mrk 273 and Mrk 273x. In the top panel, the dashed line represents the weighted average of the data points for Mrk 273 and Mrk 273x from 1994, 2000, and 2002 and the dotted lines represent a single standard deviation away from that mean. In the bottom panel, the dashed line represents the weighted average of the data points for Mrk 273 and Mrk 273x from 1994, 1998, 2002, and 2006 and the dotted lines denote one standard deviation away from the mean. Small flux increases in Mrk 273 may be observed in 2006 in the 0.5–2 keV band and in 2000 in the 2–10 keV band. The *ASCA* (1994) and *BeppoSAX* (1998) values are drawn from Iwasawa (1999) and Risaliti et al. (2000), respectively. The *Chandra* (2000) and *XMM-Newton* (2002) values are derived from our modeling of the archived spectra with the scattering model (see §5.2). The error bars to the total flux are the sums of the errors in the measured fluxes of Mrk 273 and Mrk 273x added in quadrature. A small horizontal offset was applied to the Mrk 273 data points to better display the measurement errors. Since the errors on the *BeppoSAX* measurements are not published, they are assumed to be  $\pm 20\%$  based on the results on *F05189 – 2524* by Severgnini et al. (2001).

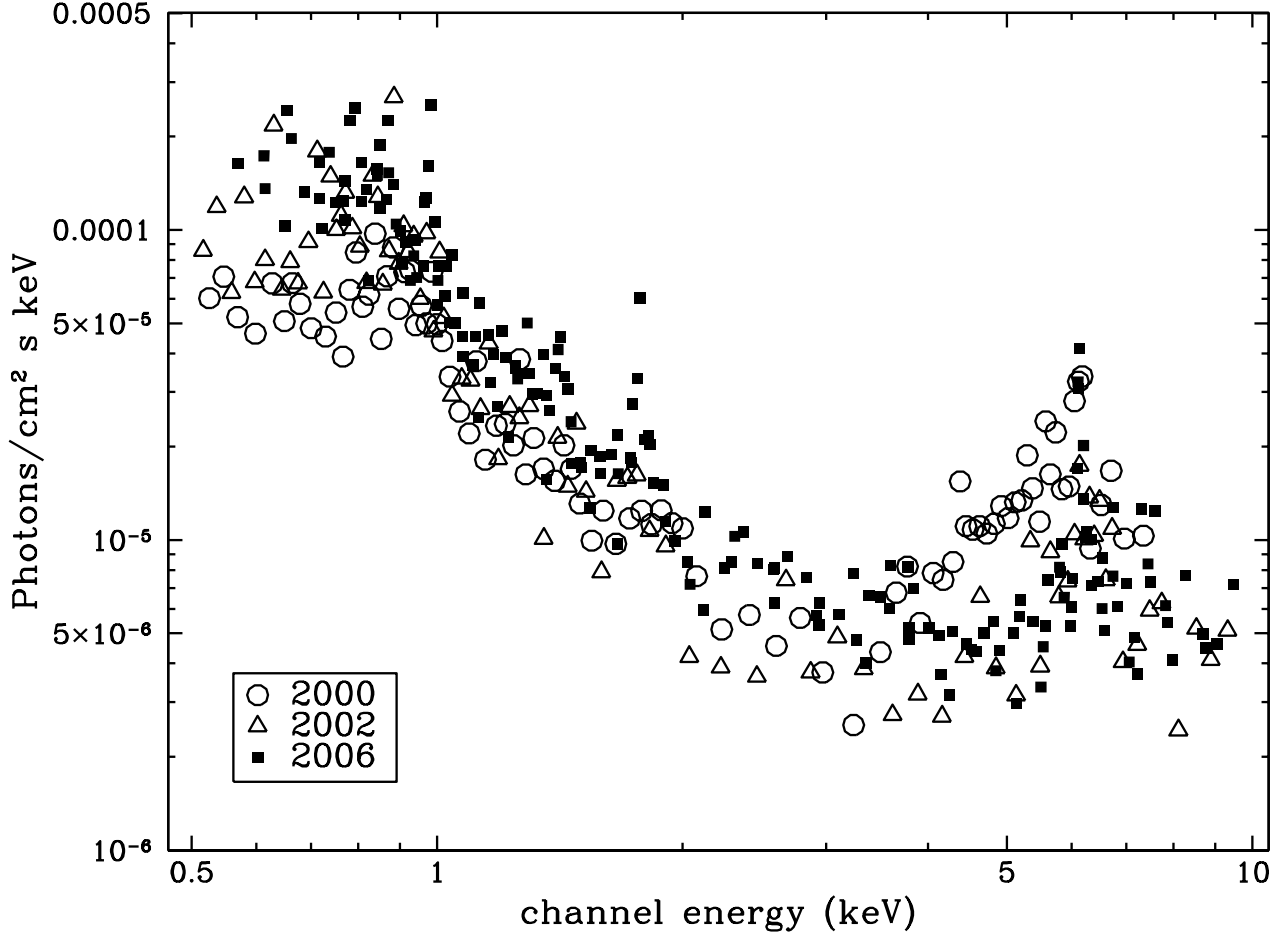


Fig. 9.— Comparison of the unfolded spectra of Mrk 273 from the 2000 *Chandra* (open circles), 2002 *XMM-Newton* (open triangles), and 2006 *Suzaku* (closed squares) observations. The unfolded spectra were created using the best-fit models to each individual spectrum. The shapes of the spectra appear consistent between 1 and 2 keV. The flux of the *Suzaku* spectrum is higher than that of the others below 1 keV, while the *Chandra* spectrum appears to be higher than the others between 4 and 6 keV. These differences are correlated with the flux variability as shown in Figure 8. This comparison also shows that the iron line at 6.4 keV is detected in all three observations. While the 2–10 keV flux variability is not very significant, the spectral shape of the source has changed between 2000 and 2006. This change may be due to the variations in the column density.

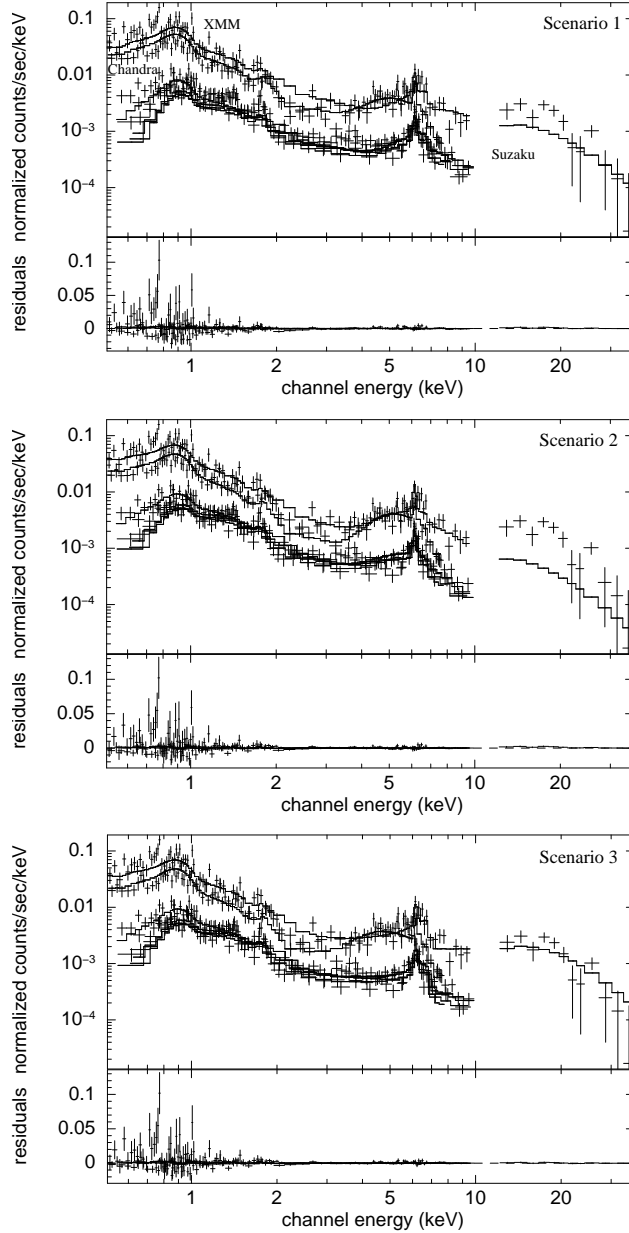


Fig. 10.— The three models to the *Chandra*-ACIS, *XMM*-Newton-EPIC pn, and *Suzaku*-XIS/PIN data used to explain the changes in the 2–10 keV spectral shape of Mrk 273: scenario 1 (top) tests only a change in the absorbing column, scenario 2 (middle) tests only a change in the intrinsic luminosity of the AGN, and scenario 3 (bottom) tests the change in the covering fraction of the absorber (see §5.2 for details). The response from each detector is folded in with the data. The horizontal axis is energy in the observer’s frame. The cross-normalization factor is assumed to be unity for *XMM*-Newton and *Chandra* with respect to *Suzaku*-XIS0. While all three models have similar reduced  $\chi^2$  values (1.76, 1.53, and 1.39 respectively), the third model provides the best-fit to the overall 0.5–40 keV spectrum. Thus, we favor the third scenario (change in the covering fraction of the absorbers) as the best explanation for the change in the 2–10 keV spectral shape of Mrk 273. Table 4 lists the results from this modeling.